Final Draft

of the original manuscript

Mossaiby, F.; Shojaei, A.; Boroomand, B.; Zaccariotto, M.; Galvanetto, U.:

Local Dirichlet-type absorbing boundary conditions for transient elastic wave propagation problems.

In: Computer Methods in Applied Mechanics and Engineering. Vol. 362 (2020) 112856.

First published online by Elsevier: 27.01.2020

https://dx.doi.org/10.1016/j.cma.2020.112856

Local Dirichlet-type absorbing boundary conditions for transient elastic wave propagation problems

Farshid Mossaiby[a], Arman Shojaei[b,*], Bijan Boroomand[c], Mirco Zaccariotto[d,e], Ugo Galvanetto[d,e]

[a]*Department of Civil Engineering, University of Isfahan, 81744-73441 Isfahan, Iran*
[b]*Institute of Materials Research, Materials Mechanics, Helmholtz-Zentrum Geesthacht, Max-Planck-Strasse 1, 21502, Geesthacht, Germany*
[c]*Department of Civil Engineering, Isfahan University of Technology, 84156-83111 Isfahan, Iran*
[d]*Industrial Engineering Department, University of Padova, v. Venezia 1, Padova 35131, Italy*
[e]*Center of Studies and Activities for Space (CISAS)-"G. Colombo", v. Venezia 15, Padova 35131, Italy*

Abstract

In this paper a new collocation technique for constructing time-dependent absorbing boundary conditions (ABCs) applicable to elastic wave motion is devised. The approach makes use of plane waves which satisfy the governing equations of motion to construct the absorbing boundary conditions. The plane waves are adjusted so that they can cope with the satisfaction of radiation boundary conditions. The proposed technique offers some advantages and exhibits the following features: it is easy to implement; its approximation scheme is local in space and time and thus it does not deal with any routine schemes such as Fourier and Laplace transform, making the method computationally less demanding; as the employed basis functions used to construct the absorbing boundary condition are residual-free, it requires neither any differential operator (to approximate the wave dispersion relation), nor any auxiliary variables; it constructs Dirichlet-type ABCs and hence no derivatives of the field variables are required for the imposition of radiation conditions. In this study, we apply the proposed technique to the solution procedure of a collocation approach based on the finite point method which proceeds in time by an explicit velocity-Verlet algorithm. It contributes to developing a consistent meshless framework for the solution of unbounded elastodynamic problems in time domain. We also apply the proposed method to a standard finite element solver.

*Corresponding author
Email address: arman.shojaei@hzg.de (Arman Shojaei)

The performance of the method in solution of some 2D examples is examined. We shall show that the method exhibits appropriate results, conserves the energy almost exactly, and it performs stably in time even in the case of long-term computations.
Keywords: unbounded domains, absorbing boundary conditions, elastic wave propagation, time domain, meshless method, finite element method

1. Introduction

The transient elastic wave propagation problems in infinite media are encountered in various fields of natural science and engineering [1]. In particular, they find several applications in soil-structure interaction analysis [2, 3] and in the simulation of earthquake ground motion [4]. The main challenge for this type of problems lies in the infinity of the media. The governing equations of the wave motion are posed on a spatial domain of infinite extent; moreover, the complexity of these problems precludes analytical solutions. The need for realistic models often compels development of a numerical solution on a bounded problem domain.

The standard numerical methods, whether mesh-based such as the finite element method (FEM) or meshless such as the finite difference method (FDM), are basically developed for bounded problem domains. The common way of tackling this problem numerically, is first to truncate the unbounded problem domain at an artificial boundary with a certain distance away from the region of interest. The region of interest is referred to as the interior domain; on the other hand, the truncated part is referred to as the exterior domain. The artificial boundary should be placed at a distance far enough so that it surrounds all the scatterers and sources of energy. In order to render the problem well-posed, it is essential to devise an appropriate mechanical model, numerical technique or absorbing boundary condition (ABC) at the truncating boundary so that the effects of the exterior region (on the interior region) can be taken into account precisely. In this sense, the technique must be capable of absorbing the incident and outgoing waves suitably through which the energy can be radiated into the exterior domain without reflecting back. The numerical solution of the bounded domain can represent that of the original unbounded domain (within the interior region) provided

that accurate and reliable boundary conditions are imposed on the artificial boundary.

Although during the last four decades a considerable number of techniques for treating wave propagation in unbounded domains have been proposed, this topic is still an open issue for the scientists [5–8]. It turns out that in some cases it is too difficult to develop a scheme that is sufficiently accurate, stable and computationally efficient and, at the same time, can be applied in conjunction with standard numerical techniques. This is more pronounced for elastodynamic problems which is the main focus of the present study [9]. Also, elastic wave problems are much more complicated than scalar wave problems in terms of the radiation condition satisfaction. This is due to the fact that elastodynamic problems are vectorial and involve more than one kind of wave [10]. To this respect, in the literature, the scalar wave propagation have been studied more widely.

In the literature of elastic wave propagation, the first attempt for developing an ABC, dates back to 1969 when the classical viscous boundary condition was introduced by Lysmer and Kuhlemeyer [11]. Since then, there has been an increasing interest in the development of new methods, and it is still an open topic of research in the field of wave motion [5, 12]. The classical ABC introduced by Engquist and Majda [13] is among the pioneering works in the literature. They proposed a method based on the local approximation of the radiation condition of increasing order (local in space and time). However, as this method involves one-way boundary operators (i.e. only along a direction normal to the boundary), it cannot avoid spurious reflections due to various wave types with different angles of incidence. The important feature of the classical ABC is that it is local in space and time. It is simple to implement in the finite element method (FEM); moreover, it is computationally cheap as long as a low order of approximation is considered (i.e. 1st or 2nd order) [14].

In general, boundary conditions that are local in space and time involve only a few points near the boundary within a small time-window [15]; yet they are not as accurate as the global approaches such as the methods based on the boundary element method (BEM) [16]. However, transient analysis of unbounded media using global approaches requires extensive computational resources [14]. To this respect, during the past decade, local methods have been receiving an increasing attention by the scientists. Classify-

ing the broad spectrum of available methods is beyond the scope of this work. The interested reader may refer to the comprehensive reviews in [17–19].

Many of the approaches are developed for time-harmonic exterior problems; for example see [20–23]. However, material non-linearity that may occur in wave motion, can be handled much more conveniently when a problem is solved in the time-domain. In the present study, the focus is on developing a technique through which the radiation condition can be satisfied directly in the time-domain. Over the past decade, the two most prominent schemes have been those based on the high-order absorbing boundary condition (high-order ABC) method [17] and those based on the perfectly matched layer (PML) method [24]. They are still actively being developed by the researchers; see for instance [25–27].

PML was originally introduced for electromagnetics by Bèrenger in 1994 [28]. Since then there have been several related reformulations of PML for other wave-type equations such as elastodynamics; for instance, see the study in [29]. A PML layer should be expanded towards the exterior domain, with a finite thickness, and it should be placed adjacent the truncating boundary of the problem. The governing equations of wave are artificially modified inside the layer. This modification is devised so that when waves travel inside the layer, they decay exponentially. In the continuous level, there is a perfect match between the PML and the interior domain through which outgoing waves, with various angles of incidence, produce zero reflection. PML introduces an artificial damping through a complex change of spatial coordinates for the wave equation in Fourier (or Laplace) space [30]. These features guarantee excellent performance of PML in theory. However, sometimes this performance might be hampered, when discretization comes into play. This lies in the sensitivity of PML to the discretization and its dependency on the introduction of ad-hoc stretching and damping profiles [9].

The first high-order ABC was proposed by Collino in 1993 [31] and then the idea was followed by other researchers; for a survey on this topic, one may refer to [10, 17]. The high-order ABC is local in space and time which is also the case for the classical ABC of Engquist and Majda [13] and Bayiss and Turkel [32]. However, unlike the classical ABC, it does not involve high-order derivatives of the main field variables. In this way, the classical ABC, in practice, can be implemented up to the second order

only; while, high-order ABC can be implemented up to a desired order. The high-order derivatives of the field variables are eliminated by introducing auxiliary variables on the truncating boundary. The methods based on high-order ABC can be implemented to any degree of accuracy, which depends on the convergence of the Padè expansion [33].

One of the restrictions of methods based on the high-order ABC is that in their design, it is not possible to include any normal derivative of an auxiliary variable on the boundary. This is due to the fact that the auxiliary variables are discretized only on the boundary. Therefore, it is only allowed to deal with tangential and temporal derivatives of the auxiliary variables. It should be remarked here that the elimination of normal derivatives of auxiliary variables is cumbersome and entails a lot of algebra in elastodynamics [9].

Each of the two schemes, high-order ABC and PML, has relative advantages. PML can usually be implemented in existing codes easier than high-order ABC. A notable disadvantage of PML, in comparison to high-order ABC, is its convergence that is not associated with a specific notion of convergence [34]. In this sense, sometimes to capture a proper accuracy by PML, it is necessary to widen the corresponding layers extensively which contributes to a considerable computational cost with respect to high-order ABC. On the other hand, high-order ABC should be applied to a fixed boundary rather than a layer. In high-order ABC by increasing the order P of the ABC the numerical solution can get closer to the exact solution up to discretization error. In high-order ABC the overhead increases linearly with P. On the basis of the studies conducted in [34], most often methods based on high-order ABC exhibit proper performance at the discrete level, provided that they have been appropriately designed at the continuous level. However, this is not generally true for PML. For more details and discussion on the comparison between these methods one may refer to [35, 36]. More recently, in the literature, there is a tendency to design new approaches that share some similarities with the features of both high-order ABC and PML, yet enjoy some of the advantages that each of them lacks; for instance see [34].

The present study aims to devise a new technique to produce ABCs suitable for transient propagation of elastic waves in unbounded domains. The work is inspired by

previous work of authors in [37] about a new way of constructing ABCs for transient scalar wave propagation problems. Here we attempt to achieve the same features for the case of elastodynamics. The proposed method is similar to the classical ABC method in terms of the simple implementation. Similar to the strategy carried out for the methods based on the classical ABC and the high-order ABC, we truncate the domain at an absorbing boundary. The ABCs are constructed by means of a simple collocation approach which is local in space and time, eliminating any routines such as Fourier and Laplace transform. The collocation approach makes use of a least square approximation over a sub-domain (so called *cloud*) centered at each points of the truncating boundary. This is similar to that of the meshless finite point method (FPM) [38, 39]. In the present study, for the sake of consistency, the solution strategy of the interior region is carried out by a simple explicit FPM solver. Similar to [37, 39], the time marching is performed using a velocity-Verlet scheme. The present collocation approach, at the absorbing boundary, approximates the solution using a series of exponential basis functions (EBFs) that satisfy the strong-form of the governing equations in space and time. EBFs are obtained in the form of plane waves whose fluctuations and directions can be adjusted and controlled such that they radiate the energy towards the exterior domain.

The way of satisfying the ABCs in time is designed so that the present method does not involve directly in the discretization scheme of the interior region. As a consequence, it can be conveniently applied to equip the existing standard numerical methods (such as FPM or FEM) for the satisfaction of the radiation boundary condition directly in the time-domain. We shall show the application of the present approach to a standard FEM solver in Sec. 4.

Likewise, the method can absorb the travelling waves with a direction normal to the absorbing boundary as well as waves with other angles of incidence. In this sense, waves with frequency and angle of incidence equal or near used plane waves are absorbed to a much higher degree. It should be remarked that in [37] a comprehensive investigation into comparison of the proposed strategy with PML and the classical 1st order ABC in terms of accuracy and efficiency (for the scalar wave motion) is conducted.

One of the appealing features of the present method is that the constructed ABCs are Dirichlet- (or first-) type and thus they can be easily imposed to the corresponding

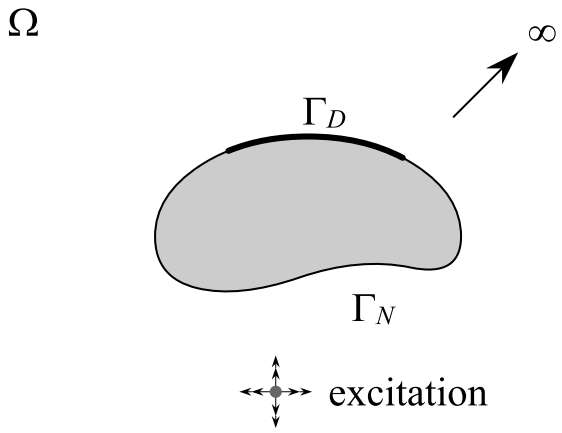

Figure 1: A general representation of an unbounded domain.

points of the absorbing boundary through a simple updating algorithm. In other words we patch the numerical solution of the near field with the semi-analytical solution of the far field, obtained by employing a series of plane waves. Such a feature makes the approach free from any spatial derivatives, even for the main field variables. We shall show that the method is capable of producing results with a suitable accuracy, and it exhibits a stable behavior even in the case of long-term computations.

The outline of the paper is as follows. In Sec. 2 the mathematical and physical descriptions of the problem are expressed. The solution strategy in different parts of the domain is presented in Sec. 3 and the way of applying the discretized formulation and forming the final system of equations are discussed. Application of the proposed method to a standard FEM solver is briefly discussed in Sec. 4. Sec. 5 explains some implementation aspects of the current work. In Sec. 6 the performance of the approach in solution of some 2D problems is examined. The final remarks made throughout the paper are summarized in Sec. 7.

2. Problem description

Let us consider a generic linear elastic unbounded domain of wave propagation Ω surrounding some scatterers (including baffles and sources) as shown in Fig. 1. We assume that the medium is homogenous and isotropic. Therefore, for any point of the

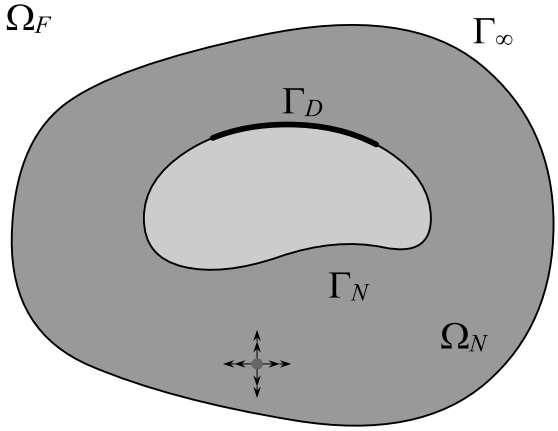

Figure 2: Specification of the computational domain and the artificial boundary.

domain $\mathbf{x} \in \Omega$, with coordinates $\mathbf{x} = \langle x, y \rangle$ with respect to the global coordinate system, the governing equation of motion at time t can be written as follows:

$$\mathbf{S}^{\mathrm{T}}\mathbf{D}\mathbf{S}\mathbf{u}(\mathbf{x}, t) + \mathbf{b}(\mathbf{x}, t) = c_d\dot{\mathbf{u}}(\mathbf{x}, t) + \rho\ddot{\mathbf{u}}(\mathbf{x}, t), \quad \mathbf{x} \in \Omega \tag{1}$$

where $\mathbf{u}$ is the displacement vector with $\langle u, v \rangle$ components respectively along the x and y directions in the global coordinate system. $\dot{\mathbf{u}}$, $\ddot{\mathbf{u}}$ and $\mathbf{b}$ are the vectors of velocity, acceleration and body forces, respectively. ρ is the density, and c_d denotes the damping coefficient. $\mathbf{S}$ is the well-known small strain operator, defined as:

$$\mathbf{S}^{\mathrm{T}} = \begin{bmatrix} \partial/\partial x & 0 & \partial/\partial y \\ 0 & \partial/\partial y & \partial/\partial x \end{bmatrix} \tag{2}$$

and $\mathbf{D}$ is the matrix of material constants; for a plane stress problem we have:

$$\mathbf{D} = \frac{E}{1-\nu^2}\begin{bmatrix} 1 & \nu & 0 \\ \nu & 1 & 0 \\ 0 & 0 & (1-\nu)/2 \end{bmatrix} \tag{3}$$

and for a plane strain problem we have:

$$\mathbf{D} = \frac{E}{(1+\nu)(1-2\nu)}\begin{bmatrix} 1-\nu & \nu & 0 \\ \nu & 1-\nu & 0 \\ 0 & 0 & (1-2\nu)/2 \end{bmatrix} \tag{4}$$

where ν is Poisson's ratio and E is Young's modulus. The strain and stress are defined (in Voigt notation) as:

$$\boldsymbol{\varepsilon} = \mathbf{S}\mathbf{u}, \quad \boldsymbol{\sigma} = \mathbf{D}\boldsymbol{\varepsilon} = \mathbf{D}\mathbf{S}\mathbf{u} \tag{5}$$

respectively. On the surface of scatterers two types of Dirichlet (constrained displacements) and Neumann (traction) conditions must be satisfied as:

$$\begin{aligned} \tilde{\mathbf{n}}\mathbf{D}\mathbf{S}\mathbf{u}(\mathbf{x}, t) &= \mathbf{t}^*(\mathbf{x}, t), \quad \mathbf{x} \in \Gamma_N \\ \mathbf{u}(\mathbf{x}, t) &= \mathbf{u}^*(\mathbf{x}, t), \quad \mathbf{x} \in \Gamma_D \end{aligned} \tag{6}$$

where Γ_D and Γ_N are Dirichlet and Neumann boundaries where the prescribed boundary displacements $\mathbf{u}^*$ and tractions $\mathbf{t}^*$ have to be imposed. Also $\tilde{\mathbf{n}}$ is a matrix containing n_x and n_y values which are components of an outward unit vector normal to the boundary, $\mathbf{n}$:

$$\tilde{\mathbf{n}} = \begin{bmatrix} n_x & 0 & n_y \\ 0 & n_y & n_x \end{bmatrix} \tag{7}$$

Moreover, the initial displacement and velocity conditions of the problem are:

$$\begin{aligned} \mathbf{u}(\mathbf{x}, 0) &= \mathbf{u}_0(\mathbf{x}) \\ \dot{\mathbf{u}}(\mathbf{x}, 0) &= \dot{\mathbf{u}}_0(\mathbf{x}) \end{aligned} \tag{8}$$

where $\mathbf{u}_0$ and $\dot{\mathbf{u}}_0$ are the given vectors of the initial conditions, respectively.

The main challenging part of the solution associated with Eq. (1) is the difficulty to cope with the infinity of the medium. To this respect, the application of standard numerical methods requires discretization of a very large portion of the unbounded domain Ω, yet this makes the approach inefficient and computationally expensive.

An appropriate strategy is to restrict the domain by specifying a *computational domain*, Ω_N, and truncating the exterior domain Ω_F using an artificial boundary Γ_∞ (see Fig. 2). This strategy converts the solution domain to a bounded one which includes the parts whose solution is mainly of concern. Γ_∞ is also referred to as the *absorbing boundary*. Ω_N is referred to as the *near field* where the solution is sought, while Ω_F is called the *far field* or the exterior domain.

We assume that the location of Γ_∞ is set so that the entire support of the body forces $\mathbf{b}$ as well as the region of damping in Eq. (1), initial conditions $\mathbf{u}_0$ and $\dot{\mathbf{u}}_0$ in Eq. (8),

and scatterers are all contained in Ω_N. Due to these assumptions, on Γ_∞ and in Ω_F the following governing equation, holds:

$$\mathbf{S}^{\mathrm{T}}\mathbf{D}\mathbf{S}\mathbf{u}(\mathbf{x},t) = \rho\ddot{\mathbf{u}}(\mathbf{x},t), \quad \mathbf{x} \in \Omega_F \tag{9}$$

It is remarkable that the exterior domain is initially assumed to be at rest.

To obtain a well-posed bounded problem domain, we introduce a simple way to construct time-dependent boundary conditions being imposed to the points at Γ_∞. In this study, the constructed ABCs are of Dirichlet type. The values of ABCs should be obtained such that the propagating waves crossing Γ_∞ can be transmitted towards the exterior domain, and no reflection back to the near field takes place. In other words, the values of ABCs should be determined so that the effects of the far field on the near field, at the truncating boundary, are taken into account properly. In this way, the solution of the bounded domain can conform suitably to that of the original domain within the sought part.

In the subsequent section, the approximation strategy for the near field and the far field are described in detail. We begin with the FPM and extend the approach to a standard FEM solver.

3. The solution strategy

The first part of the solution regards the approximation scheme in the near field. It pertains to employing the FPM approximation in space and proceeding in time with an explicit time integration scheme pursuing the study in [39]. The second part, corresponds to the construction of the ABCs for elastodynamic problems; which is the main goal of the present study. This part is tackled by a collocation technique consistent with FPM.

3.1. Near field

3.1.1. The FPM scheme

We begin with the solution recalling the weighted least square (WLS) scheme employed for FPM in the pioneer study of [38]; the reader may consult the reference

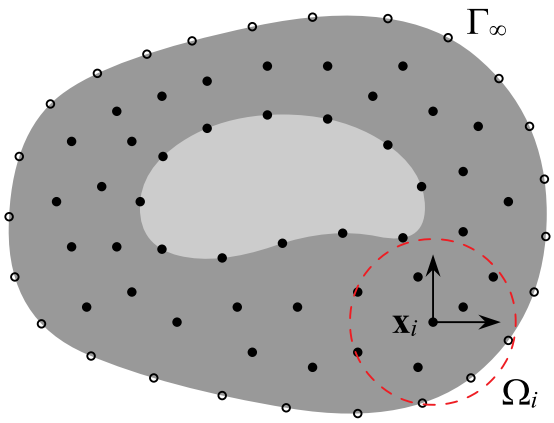

Figure 3: Discretization of the computational domain.

for more details. Let us represent the solution domain by a collection of nodes $\mathbf{x}_i$, $i = 1, 2, \ldots$, scattered within Ω_N and on the boundaries (see Fig. 3). Accordingly, the time is discretized into instants as $t_0, t_1, \ldots, t_n, t_{n+1}, \ldots$; we consider a constant time step $\Delta t = t_{n+1} - t_n$ for the discretization in time. At each node a subdomain, so called *cloud*, is centered. Ω_i indicates the neighboring nodes of $\mathbf{x}_i$, i.e., the finite region over which the unknown field variables are approximated. To each cloud Ω_i a local coordinate system with origin at $\mathbf{x}_i$ is assigned; the local axes can be parallel to those of the global coordinate system. For simplicity, we use hereafter the same notation for local and global coordinates. An unknown field variable, for instance $u(\mathbf{x}, t_n)$ (the displacement along the x-axis of the local coordinate system at time instant t_n) can be approximated locally in space by $\hat{u}^n(\mathbf{x})$ as:

$$\hat{u}^n(\mathbf{x}) = \sum_k a_k^n p_k(\mathbf{x}) = \mathbf{p}^{\mathrm{T}}(\mathbf{x})\mathbf{a}^n \tag{10}$$

recalling that here $\mathbf{x} = \langle x, y \rangle$ stands for the position with respect to the local coordinate system. In Eq. (10), $\mathbf{p}(\mathbf{x})$ denotes a vector consisting of m number of monomial bases with corresponding unknown coefficients collected in vector $\mathbf{a}^n$; the unknown coefficients must be determined in terms of the nodal values of the neighboring nodes. Considering a complete set of monomials, for a 2D problem one can choose the bases

p_k up to second order as:

$$\mathbf{p} = \langle 1, x, y, x^2, xy, y^2 \rangle, \quad m = 6 \tag{11}$$

To proceed with the WLS scheme for cloud Ω_i, it is required to sample the approximate function of field variable in Eq. (10) at the neighboring nodes (including $\mathbf{x}_i$) as:

$$\mathbf{U}^n = \begin{pmatrix} u_i^n \\ \vdots \\ u_j^n \\ \vdots \end{pmatrix} \approx \begin{pmatrix} \hat{u}^n(\mathbf{0}) \\ \vdots \\ \hat{u}^n(\mathbf{x}_{ij}) \\ \vdots \end{pmatrix} = \begin{bmatrix} \mathbf{p}^{\mathrm{T}}(\mathbf{0}) \\ \vdots \\ \mathbf{p}^{\mathrm{T}}(\mathbf{x}_{ij}) \\ \vdots \end{bmatrix} \mathbf{a}^n = \mathbf{M}\mathbf{a}^n, \quad \mathbf{x}_{ij} = \mathbf{x}_j - \mathbf{x}_i, \quad \mathbf{x}_j \in \Omega_i \tag{12}$$

where $\mathbf{M}$ and $\mathbf{a}^n$ respectively denote the moment matrix and the unknown coefficients associated with the local approximation of Ω_i. Considering n_i as the number of neighboring nodes of Ω_i and assuming that $n_i > m$, the moment matrix is no longer a square matrix; in turn, the solution of the above system of equations, for having the unknown coefficients in terms of the nodal values, entails a WLS procedure. The approximation requires an extra procedure to minimize a norm J defined by:

$$J = \sum_j w(\mathbf{x}_{ij}) \left(u_j^n - \hat{u}^n(\mathbf{x}_{ij}) \right)^2 = \sum_j w(\mathbf{x}_{ij}) \left(u_j^n - \mathbf{p}^{\mathrm{T}}(\mathbf{x}_{ij}) \mathbf{a}^n \right)^2 \tag{13}$$

where w plays the role of a weight function that must be selected properly; the above summation runs over all the neighboring nodes. In this study, as suggested in [40], the weight function is taken as:

$$w(\mathbf{x}_{ij}) = \frac{1 - \exp\left(64 - 16 \left| \frac{\mathbf{x}_j - \mathbf{x}_i}{\delta} \right|^2 \right)}{1 - \exp(64)} \tag{14}$$

in which δ is the distance of the most remote neighboring node from $\mathbf{x}_i$; when a circular shape is assumed for the cloud, it denotes the radius. To this end, minimization of J in Eq. (13), with respect to the unknown coefficients $\mathbf{a}^n$, results in the following system of equations:

$$\mathbf{A}\mathbf{a}^n = \mathbf{B}\mathbf{U}^n \tag{15}$$

where $\mathbf{A}$ is a matrix defined as:

$$\mathbf{A} = \sum_j w(\mathbf{x}_{ij}) \mathbf{p}(\mathbf{x}_{ij}) \mathbf{p}^{\mathrm{T}}(\mathbf{x}_{ij}) \tag{16}$$

and $\mathbf{B}$ is:

$$\mathbf{B} = \begin{bmatrix} w(\mathbf{0})\mathbf{p}(\mathbf{0}) & \cdots & w(\mathbf{x}_{ij})\mathbf{p}(\mathbf{x}_{ij}) & \cdots \end{bmatrix} \tag{17}$$

in which the number of columns is equal to the number of neighboring nodes n_i. According to Eq. (15), $\mathbf{a}^n$ can be found by:

$$\mathbf{a}^n = \mathbf{A}^{-1}\mathbf{B}\mathbf{U}^n \tag{18}$$

Consequently, the approximate function of the field variable $\hat{u}^n(\mathbf{x})$ can be expressed, in terms of the nodal values of the neighboring nodes of Ω_i, by substituting $\mathbf{a}^n$ from Eq. (18) for Eq. (10) as:

$$\hat{u}^n(\mathbf{x}) = \mathbf{p}^{\mathrm{T}}(\mathbf{x})\mathbf{A}^{-1}\mathbf{B}\mathbf{U}^n = \sum_j N_j(\mathbf{x})u_j^n \tag{19}$$

where $N_j(\mathbf{x})$ is the shape function of approximation corresponding to neighboring node $\mathbf{x}_j$.

3.1.2. Discretization of governing equations

For each cloud Ω_i, the unknown field variables (displacements along x and y directions of the local coordinate system) can be approximated simultaneously by $\hat{\mathbf{u}}^n(\mathbf{x}) = \langle \hat{u}^n(\mathbf{x}), \hat{v}^n(\mathbf{x}) \rangle$. The components of $\hat{\mathbf{u}}^n(\mathbf{x})$ can be found in terms of the nodal values of the neighboring nodes as described for the derivation of Eq. (19), and we have:

$$\hat{\mathbf{u}}^n(\mathbf{x}) = \mathbf{N}(\mathbf{x})\bar{\mathbf{U}}^n \tag{20}$$

where $\mathbf{N}(\mathbf{x})$ is a matrix containing the shape functions of the cloud and $\bar{\mathbf{U}}^n$ is a vector collecting the nodal values of the neighboring nodes (displacements) as follow:

$$\mathbf{N}(\mathbf{x}) = \begin{pmatrix} N_i(\mathbf{x}) & 0 & \cdots & N_j(\mathbf{x}) & 0 & \cdots \\ 0 & N_i(\mathbf{x}) & \cdots & 0 & N_j(\mathbf{x}) & \cdots \end{pmatrix}, \quad \bar{\mathbf{U}}^n = \langle u_i^n, v_i^n, \ldots, u_j^n, v_j^n, \ldots \rangle \tag{21}$$

For the nodes of the near field, the strong form of the governing equations can be discretized inserting equation Eq. (20) into Eq. (1), then we have:

$$\mathbf{S}^{\mathrm{T}}\mathbf{D}\mathbf{S}\mathbf{N}\Big|_{\mathbf{x}_i} \bar{\mathbf{U}}^n + \mathbf{b}_i^n = c_d\dot{\mathbf{u}}_i^n + \rho\ddot{\mathbf{u}}_i^n, \quad \mathbf{x}_i \in \Omega_N \tag{22}$$

where $\mathbf{b}_i^n = \mathbf{b}(\mathbf{x}_i, \mathbf{t}_n)$. In a similar manner, in view of Eq. (6), for the nodes on the Neumann boundary we have:

$$\tilde{\mathbf{n}}\mathbf{D}\mathbf{S}\mathbf{N}^{\mathrm{T}}\Big|_{\mathbf{x}_i}\bar{\mathbf{U}}^n = \mathbf{t}^*(\mathbf{x}_i, t_n), \quad \mathbf{x}_i \in \Gamma_N \tag{23}$$

and for the nodes on the Dirichlet boundary one can write:

$$\mathbf{N}(\mathbf{0})\bar{\mathbf{U}}^n = \mathbf{u}^*(\mathbf{x}_i, t_n), \quad \mathbf{x}_i \in \Gamma_D \tag{24}$$

It should be pointed out that the above procedure can be extended and applied to boundary nodes to which mixed type of boundary conditions (Dirichlet-Neumann) are imposed.

3.1.3. Time integration scheme

In this study, the time marching is performed through an explicit velocity-Verlet scheme. Having known the displacement, velocity and acceleration vectors of node $\mathbf{x}_i$ at time t_n, (i.e. $\mathbf{u}_i^n, \dot{\mathbf{u}}_i^n, \ddot{\mathbf{u}}_i^n$), one can proceed to the next time step by:

$$\begin{aligned}
\dot{\mathbf{u}}_i^{n+1/2} &= \dot{\mathbf{u}}_i^n + \frac{\Delta t}{2}\ddot{\mathbf{u}}_i^n \\
\mathbf{u}_i^{n+1} &= \mathbf{u}_i^n + \Delta t\dot{\mathbf{u}}_i^{n+1/2} \\
\dot{\mathbf{u}}_i^{n+1} &= \dot{\mathbf{u}}_i^{n+1/2} + \frac{\Delta t}{2}\ddot{\mathbf{u}}_i^{n+1}
\end{aligned} \tag{25}$$

Therefore, the displacements and velocities at time $t_{n+1} = t_n + \Delta t$ can be explicitly obtained, in terms of the values at time t_n by:

$$\begin{aligned}
\mathbf{u}_i^{n+1} &= \mathbf{u}_i^n + \Delta t\dot{\mathbf{u}}_i^n + \frac{\Delta t^2}{2}\ddot{\mathbf{u}}_i^n \\
\dot{\mathbf{u}}_i^{n+1} &= \dot{\mathbf{u}}_i^n + \frac{\Delta t}{2}\left(\ddot{\mathbf{u}}_i^n + \ddot{\mathbf{u}}_i^{n+1}\right)
\end{aligned} \tag{26}$$

It should be pointed out, having calculated $\mathbf{u}_i^{n+1}$ from the first equation, $\ddot{\mathbf{u}}^{n+1}$ can be directly calculated from the discretized form of the governing equation in Eq. (22). The time step Δt must be less than a critical time step Δt_c as follows:

$$\Delta t_c = \frac{\Delta_{\min}}{c_{\max}} \tag{27}$$

where $\Delta_{\min}$ is the minimum size of grid in the spatial discretization, and $c_{\max}$ denotes the maximum speed of sound in the material. Our experiences in the previous studies

demonstrate that the velocity-Verlet scheme can be considered as a robust and reliable approach even when the solution procedure is consisting of two different numerical approaches [41–44]. For the nodes on the boundaries (Dirichlet, Neumann and artificial boundaries) the updating of nodal values at each time step is performed by the solution of a final system of equations that will be explained in Sec. 5. For the nodes on the artificial boundary Γ_∞, to find their contributing components in the final system of equations, it is required to employ an extra collocation approach described in the subsequent subsection.

3.2. Far field

On the absorbing boundary Γ_∞, the solution is approximated by means of basis functions that satisfy the governing equation (Eq. (9)) in space and time. The way to obtain these residual-free basis functions, to adjust them for satisfaction of the radiation conditions, and to employ them in a collocation approach are described in the following subsections.

3.2.1. Residual-free exponential basis functions (EBFs)

Let us consider vector $\mathbf{f}(\mathbf{x}, t)$ as a basis function that satisfies the governing equation Eq. (9); the general form of $\mathbf{f}$ with unknown parameters can be written as:

$$\mathbf{f} = \boldsymbol{\psi} \exp(\mathrm{i}\alpha x + \mathrm{i}\beta y + \mathrm{i}\omega t), \quad \boldsymbol{\psi}(\alpha, \beta, \omega) = \begin{pmatrix} \psi_u \\ \psi_v \end{pmatrix} \tag{28}$$

where $\mathrm{i} = \sqrt{-1}$, $\alpha, \beta, \omega \in \mathbb{R}$, and $\boldsymbol{\psi}$ plays the role of an eigenvector whose size is identical to the number of displacement components. Replacement of the basis function into Eq. (9) concludes:

$$\mathbf{Q}\boldsymbol{\psi} \exp(\mathrm{i}\alpha x + \mathrm{i}\beta y + \mathrm{i}\omega t) = \mathbf{0} \tag{29}$$

where $\mathbf{Q}$ is a matrix as:

$$\mathbf{Q} = \begin{bmatrix} -D_1\alpha^2 - D_3\beta^2 + \rho\omega^2 & -(D_2 + D_3)\alpha\beta \\ -(D_2 + D_3)\alpha\beta & -D_3\alpha^2 - D_1\beta^2 + \rho\omega^2 \end{bmatrix} \tag{30}$$

Since we seek non-trivial solutions for Eq. (29) the following *characteristics* equation must hold:

$$\alpha^2\beta^2 D_1^2 + \alpha^4 D_1 D_3 - \rho\omega^2\left(\alpha^2+\beta^2\right)(D_1+D_3) + \beta^4 D_1 D_3 - \alpha^2\beta^2 D_2^2 - 2\alpha^2\beta^2 D_2 D_3 + \rho^2\omega^4 = 0 \quad (31)$$

Moreover, $\boldsymbol{\psi}$ must be obtained, in terms of the exponents, so that we have:

$$\boldsymbol{\psi} \in \text{null}(\mathbf{Q}) \quad (32)$$

in which null($\mathbf{Q}$) represents the null space of $\mathbf{Q}$. From the general form of the basis function in Eq. (28) it can be inferred that ω stands for the frequency corresponding to the temporal part, while α and β denote the fluctuation of the spatial part and thus they control the wave direction. To simplify the expression given in Eq. (31) and to get a better understanding of different influencing parameters we assume:

$$(\alpha,\beta) = \kappa(\cos\phi, \sin\phi), \quad \kappa \in \mathbb{R}, \quad -\pi < \phi \leq \pi \quad (33)$$

Hereinafter, we pursue the formulation for plane strain condition; however, the extension to plane stress condition is straightforward. Substitution of Eq. (33) in Eq. (31) leads to four roots for ω in terms of α and β; moreover, each solution is associated with an eigenvector as:

$$\begin{aligned} \omega_P &= \pm\kappa c_P, \quad \boldsymbol{\psi}_P = \begin{pmatrix} \cos\phi \\ \sin\phi \end{pmatrix} \\ \omega_S &= \pm\kappa c_S, \quad \boldsymbol{\psi}_S = \begin{pmatrix} -\sin\phi \\ \cos\phi \end{pmatrix} \end{aligned} \quad (34)$$

where $c_P = \sqrt{\frac{\lambda+2\mu}{\rho}}$, $c_S = \sqrt{\frac{\mu}{\rho}}$, λ and μ are Lamè coefficients. On the basis of Eq. (34) and Eq. (28), two types of basis functions (*modes* or plane waves) can be concluded:

$$\begin{aligned} \mathbf{f}_P &= \boldsymbol{\psi}_P \exp\left(\mathrm{i}\kappa(x\cos\phi + y\sin\phi) \pm \mathrm{i}\omega_P t\right) \\ \mathbf{f}_S &= \boldsymbol{\psi}_S \exp\left(\mathrm{i}\kappa(x\cos\phi + y\sin\phi) \pm \mathrm{i}\omega_S t\right) \end{aligned} \quad (35)$$

In fact, the first type of modes corresponds to the dilatation or pressure (P) waves and the second one corresponds to the distortional or shear (S) waves; to get more insight

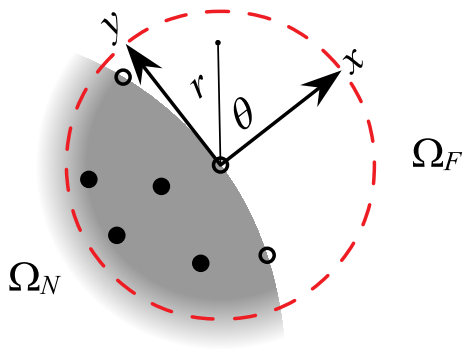

Figure 4: Schematic representation of a cloud on the absorbing boundary; the x-axis of the local coordinate system is aligned with the unit normal vector.

about the decomposition of elastodynamic waves the reader may refer to [45]. Eq. (35) considers all possible directions of propagating plane waves; however, for the approximation scheme of the nodes on Γ_∞ only the modes whose direction of propagation is towards the exterior domain must be taken into consideration.

Let us consider a portion of a generic solution domain near its absorbing boundary as shown in Fig. 4. In the discretized domain, the nodes in Ω_N and on Γ_∞ are indicated by filled and empty circles, respectively. The local coordinate system is oriented so that the x-axis is aligned with the normal vector at the absorbing boundary; furthermore, the positive direction points the exterior domain. This orientation is chosen to have a better control over the direction of the propagating waves. We proceed with the local approximation, within the cloud, applying a set of basis functions as introduced in Eq. (35):

$$\begin{aligned}\hat{\mathbf{u}}_{\infty}(\mathbf{x},t) = \sum_{k}\sum_{l}\Bigg[& a'_{k,l}\begin{pmatrix}\cos\phi_k\\ \sin\phi_k\end{pmatrix}\exp\left(\mathrm{i}\kappa_l(\eta_k - c_P t)\right) + \\ & b'_{k,l}\begin{pmatrix}-\sin\phi_k\\ \cos\phi_k\end{pmatrix}\exp\left(\mathrm{i}\kappa_l(\eta_k - c_S t)\right) + \\ & c'_{k,l}\begin{pmatrix}\cos\phi_k\\ \sin\phi_k\end{pmatrix}\exp\left(\mathrm{i}\kappa_l\eta_k + c_P t)\right) + \\ & d'_{k,l}\begin{pmatrix}-\sin\phi_k\\ \cos\phi_k\end{pmatrix}\exp\left(\mathrm{i}\kappa_l(\eta_k + c_S t)\right)\Bigg]\end{aligned} \tag{36}$$

where $\eta_k = (x\cos\phi_k + y\sin\phi_k)$; $a'_{k,l}$, $b'_{k,l}$, $c'_{k,l}$ and $d'_{k,l}$ are unknown coefficients. Moreover, we select ϕ_k and κ_l form two symmetric discrete intervals as:

$$\begin{aligned}\phi_k &\in \Delta\phi[-1,1], \quad \Delta\phi \geq 0\\ \kappa_l &\in \Delta\kappa[-1,1], \quad \Delta\kappa \geq 0\end{aligned} \tag{37}$$

In fact, $\Delta\phi$ and $\Delta\kappa$ are two influential parameters that determine the direction and frequency of the propagating plane waves. As discussed earlier, the right hand side of Eq. (36) includes the general form of all possible modes of the solution. It is notable that taking $\phi_k = 0$ (or close to that) leads to plane waves whose direction is aligned with the x-axis. Since the positive x-direction is taken towards the exterior domain, the first two terms of the series in Eq. (36) represent outgoing waves, while the last two terms represent incoming waves. Therefore, the incoming plane waves must vanish to prevent reflections of energy from the boundary towards the near field. To this end, by taking $c'_{k,l} = d'_{k,l} = 0$ the approximation function of displacements in Eq. (36) reduces to:

$$\begin{aligned}\hat{\mathbf{u}}_{\infty}(\mathbf{x},t) = \sum_{k}\sum_{l}\Bigg[& a'_{k,l}\begin{pmatrix}\cos\phi_k\\ \sin\phi_k\end{pmatrix}\exp\left(\mathrm{i}\kappa_l(\eta_k - c_P t)\right) + \\ & b'_{k,l}\begin{pmatrix}-\sin\phi_k\\ \cos\phi_k\end{pmatrix}\exp\left(\mathrm{i}\kappa_l(\eta_k - c_S t)\right)\Bigg]\end{aligned} \tag{38}$$

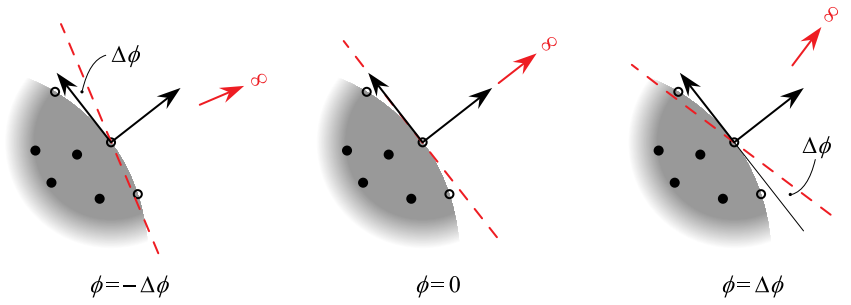

Figure 5: The propagation region of outgoing waves for different values of ϕ.

and it can be stated in the polar coordinate system, $\langle x, y\rangle = r\langle\cos\theta, \sin\theta\rangle$ and $-\pi < \theta \leq \pi$ as:

$$\begin{aligned}\hat{\mathbf{u}}_\infty(r,\theta) = \sum_k \sum_l \Bigg[& a'_{k,l} \begin{pmatrix} \cos\phi_k \\ \sin\phi_k \end{pmatrix} \exp\left(\mathrm{i}\kappa_l(r\cos\theta\cos\phi_k + r\sin\theta\sin\phi_k - c_P t)\right) + \\ & b'_{k,l} \begin{pmatrix} -\sin\phi_k \\ \cos\phi_k \end{pmatrix} \exp\left(\mathrm{i}\kappa_l(r\cos\theta\cos\phi_k + r\sin\theta\sin\phi_k - c_S t)\right) \\ = \sum_k \sum_l \Bigg[& a'_{k,l} \begin{pmatrix} \cos\phi_k \\ \sin\phi_k \end{pmatrix} \exp\left(\mathrm{i}\kappa_l(r\cos(\theta-\phi_k) - c_P t)\right) + \\ & b'_{k,l} \begin{pmatrix} -\sin\phi_k \\ \cos\phi_k \end{pmatrix} \exp\left(\mathrm{i}\kappa_l(r\cos(\theta-\phi_k) - c_S t)\right) \Bigg]\end{aligned} \tag{39}$$

Since c_P, c_S and r are all positive, we can conclude that the terms of the above series play the role of outgoing waves (towards the exterior domain) provided that the following condition is observed:

$$\cos\left(\phi_k - \theta\right) > 0 \tag{40}$$

which concludes:

$$-\frac{\pi}{2} + \phi_k < \theta < \frac{\pi}{2} + \phi_k \tag{41}$$

In fact, the above region indicates a half plane perpendicular to a normal vector making an angle equal to ϕ_k with the x-axis of the local coordinate system. Fig. 5 illus-

trates that the half plane rotates by changing the value of ϕ_k. On the basis of Eq. (37), we choose a set of values for ϕ_k within an interval $[-\Delta\phi, \Delta\phi]$. Therefore, the plane waves of the series in Eq. (38) construct an approximate solution that guides the waves crossing Γ_∞ (incident from the near field) towards their corresponding half planes; in this way, the radiation condition can be satisfied. As a consequence, thanks to the considered orientation for the local coordinate system, a small angle close to zero for $\Delta\phi$ must be selected to guarantee the absorption of energy and prevent spurious reflection of waves from the boundary. We shall discuss about the implementation aspects as well as selection of the parameters in the following sections.

3.2.2. The approximation scheme of far field

The employed approximation scheme of Γ_∞ is quite similar to that of FPM. Let us again consider a cloud, centered at $\mathbf{x}_i$, shown in Fig. 4 as a generic cloud on Γ_∞. Within the cloud, the approximate function of displacement, introduced in Eq. (36), can be rewritten in the following form:

$$\hat{\mathbf{u}}_\infty(\mathbf{x}, t) = \begin{pmatrix} \hat{u}_\infty \\ \hat{v}_\infty \end{pmatrix}(\mathbf{x}, t) = \sum_k a_{\infty,k} \mathbf{p}_{\infty,k}(\mathbf{x}, t) \tag{42}$$

where $\mathbf{p}_{\infty,k}$ denotes the k-th basis function with the corresponding unknown coefficient $a_{\infty,k}$; it should be recalled that coordinates $\mathbf{x}$ are measured with respect to the local oriented coordinate system. In this way, we approximate the velocity separately employing a set of basis functions, the first time derivatives of the basis functions in Eq. (42), as:

$$\hat{\dot{\mathbf{u}}}_\infty(\mathbf{x}, t) = \begin{pmatrix} \hat{\dot{u}}_\infty \\ \hat{\dot{v}}_\infty \end{pmatrix}(\mathbf{x}, t) = \sum_k b_{\infty,k} \dot{\mathbf{p}}_{\infty,k}(\mathbf{x}, t) \tag{43}$$

where $b_{\infty,k}$ denotes the corresponding unknown coefficient. Since the employed collocation approach is local in space and time, at each time step we reset the time and assume that the approximation is valid for a local time interval $t \in [0, \Delta t]$. In this way, we interpolate the field variables (displacements) and their first derivations in time (velocities), at n-th time step, by:

$$\hat{\mathbf{u}}^n_\infty(\mathbf{x}, t) = \mathbf{P}^{\mathrm{T}}_\infty(\mathbf{x}, t)\mathbf{a}^n_\infty \tag{44}$$

and consequently:

$$\hat{\mathbf{u}}^n_\infty(\mathbf{x},t) = \dot{\mathbf{P}}^{\mathrm{T}}_\infty(\mathbf{x},t)\mathbf{b}^n_\infty \tag{45}$$

where $\mathbf{P}_\infty$ and $\mathbf{a}^n_\infty$ are:

$$\begin{aligned}\mathbf{P}^{\mathrm{T}}_\infty(\mathbf{x},t) &= \begin{bmatrix}\mathbf{p}_{\infty,1} & \mathbf{p}_{\infty,2} & \cdots & \mathbf{p}_{\infty,m_\infty}\end{bmatrix}(\mathbf{x},t)\\ \mathbf{a}^n_\infty &= \langle a^n_1, a^n_2, \dots, a^n_{m_\infty}\rangle\end{aligned} \tag{46}$$

and similarly we have:

$$\begin{aligned}\dot{\mathbf{P}}^{\mathrm{T}}_\infty(\mathbf{x},t) &= \begin{bmatrix}\dot{\mathbf{p}}_{\infty,1} & \dot{\mathbf{p}}_{\infty,2} & \cdots & \dot{\mathbf{p}}_{\infty,m_\infty}\end{bmatrix}(\mathbf{x},t)\\ \mathbf{b}^n_\infty &= \langle b^n_1, b^n_2, \dots, b^n_{m_\infty}\rangle\end{aligned} \tag{47}$$

The summations in Eqs. (44) and (45) run over m_∞ basis functions; in fact, Eqs. (44) and (45) are the counterparts of Eq. (10) in the FPM approximation scheme.

Hereinafter, the goal is to find the unknown coefficients in terms of the nodal values (including displacements and velocities). Similar to Eq. (12), we sample the approximate function in Eqs. (44) and (45) at the neighboring nodes (recalling that at the beginning of n-th step we set $t = 0$) as:

$$\bar{\mathbf{G}}^n = \begin{pmatrix}\mathbf{g}^n_i\\ \vdots\\ \mathbf{g}^n_j\\ \vdots\end{pmatrix} = \begin{pmatrix}\mathbf{T}\mathbf{u}^n_i\\ \vdots\\ \mathbf{T}\mathbf{u}^n_j\\ \vdots\end{pmatrix} \approx \begin{bmatrix}\mathbf{P}^{\mathrm{T}}_\infty(\mathbf{0},0)\\ \vdots\\ \mathbf{P}^{\mathrm{T}}_\infty(\mathbf{x}'_{ij},0)\\ \vdots\end{bmatrix}\mathbf{a}^n_\infty = \mathbf{M}_\infty\mathbf{a}^n_\infty, \quad \mathbf{x}'_{ij} = \mathbf{T}\mathbf{x}_{ij}, \quad \mathbf{x}_j \in \Omega_i \tag{48}$$

and accordingly:

$$\dot{\bar{\mathbf{G}}}^n = \begin{pmatrix}\dot{\mathbf{g}}^n_i\\ \vdots\\ \dot{\mathbf{g}}^n_j\\ \vdots\end{pmatrix} = \begin{pmatrix}\mathbf{T}\dot{\mathbf{u}}^n_i\\ \vdots\\ \mathbf{T}\dot{\mathbf{u}}^n_j\\ \vdots\end{pmatrix} \approx \begin{bmatrix}\dot{\mathbf{P}}^{\mathrm{T}}_\infty(\mathbf{0},0)\\ \vdots\\ \dot{\mathbf{P}}^{\mathrm{T}}_\infty(\mathbf{x}'_{ij},0)\\ \vdots\end{bmatrix}\mathbf{b}^n_\infty = \dot{\mathbf{M}}_\infty\mathbf{b}^n_\infty \tag{49}$$

where $\mathbf{T}$ is a rotation matrix, using for transformation from the global coordinate system to the local one, as:

$$\mathbf{T} = \begin{bmatrix}n_x & n_y\\ -n_y & n_x\end{bmatrix} \tag{50}$$

Assuming $n_i < m_\infty$, on the basis of Eqs. (48) and (48), the unknown coefficients $\mathbf{a}_\infty^n$ and $\mathbf{b}_\infty^n$ can be found respectively in terms of $\bar{\mathbf{G}}^n$ and $\dot{\bar{\mathbf{G}}}^n$ by:

$$\mathbf{a}_\infty^n = \mathbf{M}_\infty^+ \bar{\mathbf{G}}^n \tag{51}$$

and:

$$\mathbf{b}_\infty^n = \dot{\mathbf{M}}_\infty^+ \dot{\bar{\mathbf{G}}}^n \tag{52}$$

where the superscript '+' stands for the Moor-Penrose generalized inverse; the above equations are the counterparts of Eq. (18). By substitution of $\mathbf{a}_\infty^n$ and $\mathbf{b}_\infty^n$ from Eqs. (51) and (52) for Eqs. (44) and (45) respectively we have:

$$\hat{\mathbf{u}}_\infty^n(\mathbf{x}, t) = \mathbf{P}_\infty^{\mathrm{T}}(\mathbf{x}, t)\mathbf{M}_\infty^+ \bar{\mathbf{G}}^n = \mathbf{N}_\infty(\mathbf{x}, t)\bar{\mathbf{G}}^n \tag{53}$$

and:

$$\dot{\hat{\mathbf{u}}}_\infty^n(\mathbf{x}, t) = \dot{\mathbf{P}}_\infty^{\mathrm{T}}(\mathbf{x}, t)\dot{\mathbf{M}}_\infty^+ \dot{\bar{\mathbf{G}}}^n = \dot{\mathbf{N}}_\infty(\mathbf{x}, t)\dot{\bar{\mathbf{G}}}^n \tag{54}$$

where $\mathbf{N}_\infty$ and $\dot{\mathbf{N}}_\infty$ are two matrices including all the shape functions of the local approximation. Let us assume that at the beginning of n-th step the values of $\bar{\mathbf{G}}^n$ and $\dot{\bar{\mathbf{G}}}^n$ are known, since we are dealing with an explicit time marching in the near field. According to Eqs. (53) and Eq. (54), one can find the nodal values of $\mathbf{x}_i$ at the next time step, with respect to the local coordinate system, by:

$$\mathbf{g}_i^{n+1} = \mathbf{N}_\infty(\mathbf{0}, \Delta t)\bar{\mathbf{G}}^n \tag{55}$$

and:

$$\dot{\mathbf{g}}_i^{n+1} = \dot{\mathbf{N}}_\infty(\mathbf{0}, \Delta t)\dot{\bar{\mathbf{G}}}^n \tag{56}$$

Finally, the nodal values of $\mathbf{x}_i$ with respect to the orientation of the global coordinate system at time instant t^{n+1} can be found by:

$$\mathbf{u}_i^{n+1} = \mathbf{T}^{-1}\mathbf{g}_i^{n+1} \tag{57}$$

and:

$$\dot{\mathbf{u}}_i^{n+1} = \mathbf{T}^{-1}\dot{\mathbf{g}}_i^{n+1} \tag{58}$$

The terms of the above equation will be a part of the final system of equations explained in the subsequent section.

In the solution procedure, the required terms in the approximation of clouds are basically the terms $\mathbf{N}(\mathbf{x})$ in Eq. (20) as well as $\mathbf{N}_\infty(\mathbf{0}, \Delta t)$ and $\dot{\mathbf{N}}_\infty(\mathbf{0}, \Delta t)$ in Eqs. (55) and (56). It is worthwhile to mention that these terms can be calculated once at the beginning of the simulation. This lies in the fact that moment matrices $\mathbf{M}$ in Eq. (12), $\mathbf{M}_\infty$ and $\dot{\mathbf{M}}_\infty$ in Eqs. (48) and Eq. (49) are obtained independent of time; this feature culminates in a significant reduction in the computational cost.

3.3. Final system of equations

Here we discuss the formation of the final system of equations making use of the discretized equations developed earlier. Let $\mathbf{K}$, $\tilde{\mathbf{U}}$, and $\mathbf{F}$ be respectively the coefficient matrix, the vector of displacements, and the vector of known values for the global system of equations. Therefore, at n-th time step the solver can advance to the next time step by the solution of the following linear system of equations:

$$\mathbf{K}\tilde{\mathbf{U}}^{n+1} = \mathbf{F}^n \tag{59}$$

According to the position of a node, the corresponding rows of $\mathbf{K}$ and $\mathbf{F}^n$ should be filled out. For a node $\mathbf{x}_i$ in the near field, in view of Eq. (22) and Eq. (25), we have:

$$\mathbf{u}_i^{n+1} = \mathbf{u}_i^n + \left(\Delta t - \frac{c_d}{2\rho}\Delta t^2\right)\dot{\mathbf{u}}_i^n + \frac{\Delta t^2}{2\rho}\left(\mathbf{S}^{\mathrm{T}}\mathbf{D}\mathbf{S}\mathbf{N}\Big|_{\mathbf{x}_i}\bar{\mathbf{U}}^n + \mathbf{b}_i^n\right), \quad \mathbf{x}_i \in \Omega_N \tag{60}$$

The left hand side of the above equation should be arranged in the corresponding rows of $\mathbf{K}$, and the right hand side, consisting of known values at the beginning of n-th step, should be appropriately placed into the corresponding arrays of $\mathbf{F}^n$. The same procedure applies to nodes on Neumann and Dirichlet boundaries; on the basis of Eqs. (23) and (24), we have:

$$\begin{aligned} \tilde{\mathbf{n}}\mathbf{D}\mathbf{S}\mathbf{N}^{\mathrm{T}}\Big|_{\mathbf{x}_i}\bar{\mathbf{U}}^{n+1} &= \mathbf{t}^*(\mathbf{x}_i, t_{n+1}), \quad \mathbf{x}_i \in \Gamma_N \\ \mathbf{N}(\mathbf{0})\bar{\mathbf{U}}^{n+1} &= \mathbf{u}^*(\mathbf{x}_i, t_{n+1}), \quad \mathbf{x}_i \in \Gamma_D \end{aligned} \tag{61}$$

For nodes on the absorbing boundary the following equation, based on Eq. (57), applies:

$$\mathbf{u}_i^{n+1} = \mathbf{T}^{-1}\mathbf{N}_\infty(\mathbf{0}, \Delta t)\bar{\mathbf{G}}^n, \quad \mathbf{x}_i \in \Gamma_\infty \tag{62}$$

Having updated the displacements, the solver can update the velocities considering Eq. (22) and Eq. (25) for nodes in the near field as:

$$\dot{\mathbf{u}}_i^{n+1} = \frac{1}{1+\frac{\Delta t c_d}{2\rho}} \left(\dot{\mathbf{u}}_i^n + \frac{\Delta t}{2}\ddot{\mathbf{u}}_i^n + \frac{\Delta t}{2\rho}\mathbf{S}^{\mathrm{T}}\mathbf{D}\mathbf{S}\mathbf{N}\Big|_{\mathbf{x}_i} \bar{\mathbf{U}}^{n+1} + \frac{\Delta t}{2\rho}\mathbf{b}_i^{n+1} \right), \quad \mathbf{x}_i \in \Omega_N \tag{63}$$

and, in view of Eq. (58), for nodes on the absorbing boundary we have:

$$\dot{\mathbf{u}}_i^{n+1} = \mathbf{T}^{-1}\dot{\mathbf{N}}_\infty(\mathbf{0}, \Delta t)\bar{\dot{\mathbf{G}}}^n, \quad \mathbf{x}_i \in \Gamma_\infty \tag{64}$$

It should be pointed out the major part of the final system of equations is formed by Eq. (60) and Eq. (62) which are uncoupled equations; therefore, the system in Eq. (59) can be condensed to a much smaller one containing only the equations of nodes close to Dirichlet and Neumann boundaries; the reader may refer to [39] for more details.

Remark 1

It is worth noting that the approach described is applicable to 3D problems as well. To do this, one must consider a 3D wave basis of the form $\boldsymbol{\psi}\exp(\mathrm{i}\alpha x + \mathrm{i}\beta y + \mathrm{i}\gamma z + \mathrm{i}\omega t)$ in place of Eq. (28). The characteristic equation as well as $\boldsymbol{\psi}$ can be obtained as before. The satisfaction of the radiation condition should be done in half planes, perpendicular to the x-axis of the local coordinate system. This entails further considerations that will be the topic of future studies.

4. Application to a FEM solver

In this section, we discuss the applicability of the proposed method to a standard FEM solver, since FEM is a very popular solution method for many structural problems involving infinite domains. It is worth noting that we have equipped FEM with a strategy similar to that of the proposed method for scalar wave propagation problems [37]. To complete our discussion in this paper, we briefly devise a similar approach for unbounded elastodynamic problems. Assuming that at the n-th step the solver has the

nodal values of the system including the displacements, the velocities and the accelerations (i.e. $\tilde{\mathbf{U}}^n$, $\tilde{\dot{\mathbf{U}}}^n$ and $\tilde{\ddot{\mathbf{U}}}^n$), one may use the discrete governing equation of FEM, i.e.:

$$\tilde{\mathbf{M}}\tilde{\ddot{\mathbf{U}}}^{n+1} + \tilde{\mathbf{C}}\tilde{\dot{\mathbf{U}}}^{n+1} + \tilde{\mathbf{K}}\tilde{\mathbf{U}}^{n+1} = \tilde{\mathbf{F}}^{n+1} \tag{65}$$

to advance to $n+1$-th step using the following velocity-Verlet equations:

$$\tilde{\mathbf{U}}^{n+1} = \tilde{\mathbf{U}}^n + \Delta t\tilde{\dot{\mathbf{U}}}^n + \frac{\Delta t^2}{2}\tilde{\ddot{\mathbf{U}}}^n \tag{66}$$

$$\tilde{\dot{\mathbf{U}}}^{n+1} = \left(\mathbf{I} + \frac{\Delta t}{2}\tilde{\mathbf{M}}^{-1}\tilde{\mathbf{C}}\right)^{-1}\left[\tilde{\dot{\mathbf{U}}}^n + \frac{\Delta t}{2}\left(\tilde{\ddot{\mathbf{U}}}^n + \tilde{\mathbf{M}}^{-1}\left[\tilde{\mathbf{F}}^{n+1} - \tilde{\mathbf{K}}\tilde{\mathbf{U}}^{n+1}\right]\right)\right] \tag{67}$$

In the above equations, $\tilde{\mathbf{M}}$, $\tilde{\mathbf{C}}$ and $\tilde{\mathbf{K}}$ are the usual mass, damping and stiffness matrices of FEM. A step-by-step procedure for the solution of unbounded elastodynamic problems in FEM is depicted in Alg. 1. It is noteworthy that the proposed method does not involve directly in the discretization scheme of FEM.

5. Numerical implementation

The numerical implementation of the present method is a straightforward task as the original formulation of FPM (and FEM) is preserved and a consistent formulation for the radiative boundaries is proposed. Hereinafter, we focus on the FPM, but the reader may note similarities to the FEM implementation, as described in the previous section. The implementation mainly pertains to representation of the solution domain by distribution of nodes on the computational domain, specifying the radiative boundaries, allocation of a cloud to each node, construction of shape functions at the beginning of the simulation, and advancing in time by the procedure described in Sec. 3.3.

The local approximation in each cloud must be taken over a sufficient number of neighboring nodes. In the Sec. 6, all the examples are solved using a uniform grid for domain discretization and taking a circular region with radius of $\delta = 3\Delta x$ for each cloud; here Δx stands for the grid spacing. A complete set of polynomial basis functions up to second order is considered for the WLS approximation scheme of the clouds in the near field. To select a proper set of EBFs for the approximation scheme of the far field, we use the recommendations in [46].

Algorithm 1 The procedure for the FEM solution of unbounded elastodynamic problems.

Specify the computational domain, Ω_N
Discretize the computational domain using a standard FEM mesh
Construct the standard FEM stiffness, damping and mass matrices, $\tilde{\mathbf{K}}$, $\tilde{\mathbf{C}}$ and $\tilde{\mathbf{M}}$
Identify nodes on the absorbing boundaries, Γ_∞
for all nodes $\mathbf{x}_i$ on Γ_∞ **do**
    Build the cloud Ω_i, i.e. find nodes $\mathbf{x}_j$ such that $\|\mathbf{x}_j - \mathbf{x}_i\| \leq \delta$
    Calculate and store $\mathbf{N}_\infty(\mathbf{0}, \Delta t)$ and $\dot{\mathbf{N}}_\infty(\mathbf{0}, \Delta t)$ for Ω_i using Eqs. (55) and (56)
end for
Initialize $\tilde{\mathbf{U}}^0$ and $\dot{\tilde{\mathbf{U}}}^0$ from the initial conditions
$n \leftarrow 1$
repeat
    $t \leftarrow n\Delta t$
    Calculate $\tilde{\mathbf{U}}^{n+1}$ using Eq. (66)
    for all nodes $\mathbf{x}_i$ on Γ_∞ **do**
        Update $\tilde{\mathbf{U}}_i^{n+1}$ using Eq. (57)
    end for
    Calculate $\dot{\tilde{\mathbf{U}}}^{n+1}$ using Eq. (67)
    for all nodes $\mathbf{x}_i$ on Γ_∞ **do**
        Update $\dot{\tilde{\mathbf{U}}}_i^{n+1}$ using Eq. (58)
    end for
    $n \leftarrow n + 1$
until $t = T$

In the present study, in line with the description given in Eq. (41) and Fig. 5, ϕ_k is selected from a discrete range (symmetric and with regular subdivisions) as in Eq. (37). In all examples, we make use of 5 angles for ϕ; furthermore, we take $\Delta\phi = \pi/8$ as our experiences have shown that it is an optimal selection to transmit the arriving waves at the boundary towards the exterior domain.

The other parameter is κ_l in Eq. (33) that influences the fluctuation of plane waves in space and time. As described earlier this parameter is also selected form a discrete interval, as in Eq. (37), with regular subdivisions. For proper selection of $\Delta\kappa$, inspired by the study conducted in [47, 48], we look into the well-known sampling theorem in the field of signal processing [49]. In a nutshell, on the basis of the sampling theorem a signal (band limited) can be fully reconstructed provided that it is sampled at a rate at least twice the highest frequency content of the signal. To this respect, in the present method $\Delta\kappa$ is the maximum value of frequency for the spatial part of plane waves. Consequently, the maximum values of frequency for the temporal parts for pressure and shear waves are $\Delta\kappa c_P$ and $\Delta\kappa c_S$, respectively (see Eq. (34)). Let Δx and Δt_c be the space between sampling points (in space and time), hence the maximum proper value for $\Delta\kappa$ can be found as follows:

$$0 < \Delta\kappa < \min\left(\frac{\pi}{\Delta x}, \frac{\pi}{c_S \Delta t_c}, \frac{\pi}{c_P \Delta t_c}\right) \tag{68}$$

Since $c_P > c_S$, combination of the above equation and Eq. (27) leads to:

$$0 < \Delta\kappa < \frac{\pi}{\Delta x} \tag{69}$$

in which $\Delta_{\min}$ and $c_{\max}$ in Eq. (27) is taken equal to Δx and c_P.

The proposed methods was implemented in Julia. Julia is a free, open source, high-level, general-purpose programming language designed for high performance computing and simplicity of use [50]. Julia has several add-on packages, making available to the user a broad range of algorithms. We have, for example, employed the `NearestNeighbors` package to accelerate the process of finding the neighboring nodes to specify the clouds. This package is based on a k-d tree, which reduces the computational cost of finding neighbors from $\mathcal{O}(N^2)$ to $\mathcal{O}(N \log N)$ in which N is the number of nodes in the domain. See [51] for more details. Also, to avoid calculating the

Moore–Penrose pseudo-inverses explicitly, we have chosen a technique described in [52], where we employ the backslash ('\') operator in Julia to calculate the product of the pseudo-inverse of a matrix and a vector / matrix.

It is worth noting that while the formulation here is presented using complex numbers, the whole solution can be easily done using real numbers. This is conveniently accomplished using the well-known Euler's formula. This makes the implementation of the method easier in the existing codes, as some libraries used in the codes are available for real numbers only. The developed code also uses this technique, despite the fact that Julia seamlessly supports complex numbers.

6. Numerical examples

This section is devoted to scrutinize the performance of the proposed approach by solving some numerical examples. The examples are performed with the same set of parameters (for the absorption of energy) as described in Sec. 5 and are discretized through a Cartesian equally spaced grid of nodes.

In the examples, the wave motion is generated by prescribing initial values (displacement or velocity) for the system. The body force and the damping coefficient in Eq. (1) are taken equal to zero. Inspired by other studies about elastic wave propagation [10, 53], the accuracy and stability of the numerical solution is evaluated by calculating the following expression numerically:

$$\Pi(t) = \frac{1}{2}\int_{\Omega_N} \boldsymbol{\varepsilon}^{\mathrm{T}}\boldsymbol{\sigma}\mathrm{d}\Omega + \frac{1}{2}\int_{\Omega_N} \rho\dot{\mathbf{u}}^{\mathrm{T}}\dot{\mathbf{u}}\mathrm{d}\Omega \tag{70}$$

where Π is the total mechanical energy in the near field. In fact, the evaluation of accuracy at the level of energy is a proper choice since it is concluded form an integration over spatial and time derivatives of the field variables in the whole computational domain. It should be pointed out that the examples are set up in a dimensionless system.

6.1. Example 1: wave motion in an unbounded domain

Part A: FPM solution

The purpose in this example is to check the performance of the present method in the case of a 2D unbounded problem domain. The material properties are $\rho = 1$,

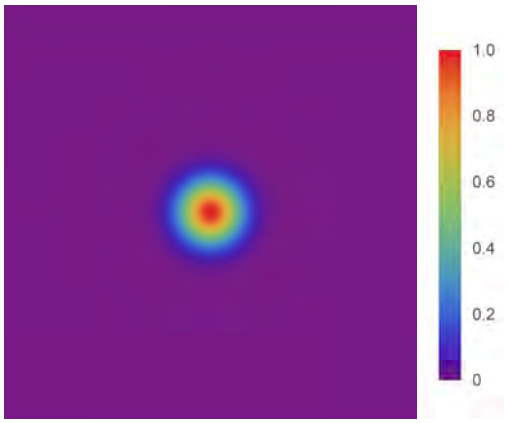

Figure 6: The initial condition in Example 1; the figure shows the displacement along the x-axis, u, taking $\Delta x = 0.004$.

$E = 10\,000$ and $\nu = 0.3$. We consider a square region $\mathbf{x} \in (-0.5, 0.5) \times (-0.5, 0.5)$ as the near field and the corresponding artificial boundary is placed at the borders; i.e., the four sides of the square. The domain is excited by prescribing an initial displacement (in the form of a truncated Gaussian bell shape) centered at $\langle 0, 0 \rangle$ to the system along both the x and y axes as:

$$u_0(\mathbf{x}) = v_0(\mathbf{x}) = \exp\left[-200\left(x^2 + y^2\right)\right] \quad \text{for } \sqrt{x^2 + y^2} \leq \frac{1}{4} \tag{71}$$

The contour plot of the initial condition, displacement along the x-axis, is depicted in Fig. 6.

To get a better understanding of the accuracy and validate the results, we consider the solution of an extended bounded domain as the reference solution. We take a square region $\mathbf{x} \in [-6, 6] \times [-6, 6]$ as the extended domain, which is discretized into 2 253 001 nodes with a regular spacing equal to $\Delta x = 0.004$. The extended domain is excited by the same initial conditions described in Eq. (71). Moreover, a homogenous Neumann condition (traction free) for the boundaries of the extended domain is taken into account.

For the spatial discretization of proposed model, two different grid sizes $\Delta x = 0.004$ and $\Delta x = 0.01$ are employed which results in 63 001 and 10 201 nodes, respectively. To proceed in time, we consider a time increment of $\Delta t = 5 \times 10^{-6}$. The wave motion in the extended domain is taken as the reference solution for a time duration $T = 0.015$; the

wave front does not reach to the borders of the extended domain in this time duration. Therefore the calculations are performed over 3000 time steps.

In Fig. 7, by plotting the contours of displacement along the x-axis at six different time instants, the propagation of the pulse is presented. We show the results of the extended domain only within the computational domain of the present model, hence the results can be easily compared. The results indicate that by time $t = 0.00375$ although the wave has crossed the border, it keeps propagating with a shape similar to that of the reference solution. By time $t = 0.01$ there is a good agreement between the solution obtained by the present model and the reference one. At the last time instant, $t = 0.015$, the reference solution indicates that majority of the pulse has already left the domain. Moreover, the solution obtained by the present model reveals that there is no significant spurious propagating waves back to the computational domain from the absorbing boundaries, as long as the grid is fine enough. The results, corresponding to the last time instant, illustrate that the magnitude range of the remaining waves is very small (in comparison to the pulse magnitude at $t = 0$, see Fig. 6) and no accountable reflections from the border can be observed when $\Delta x = 0.004$. As a consequence applying a finer grid culminates in less spurious reflections and a higher level of accuracy.

For further evaluation and getting more insight into the accuracy, the variation of energy for both models, in view of Eq. (70), is presented in Fig. 8. Recall that the integration for both models is done over the near field of the present model, $\mathbf{x} \in (-0.5, 0.5)\times(-0.5, 0.5)$. To check the stability, the calculation of energy for the present approach is done up to 10 000 steps. It should be pointed out that the energy is normalized with respect to the energy of the system at the beginning of the simulation, Π^0. It can be inferred that as time goes by, the energy is dissipating from the computational domain of the present model monotonically (i.e. $\mathrm{d}\Pi/\mathrm{d}t \leq 0$) having an excellent match with the reference solution. In fact, the obtained results for energy approve the conclusions made for the results in Fig. 7. Meanwhile, the trend of energy dissipation is captured so that no instability, due to long-term computations, occurs.

For further investigation, we check the convergence of the present model to the reference solution. Fig. 9 illustrates the variation of absolute difference between the normalized energy obtained by the present model and that of the reference solution in

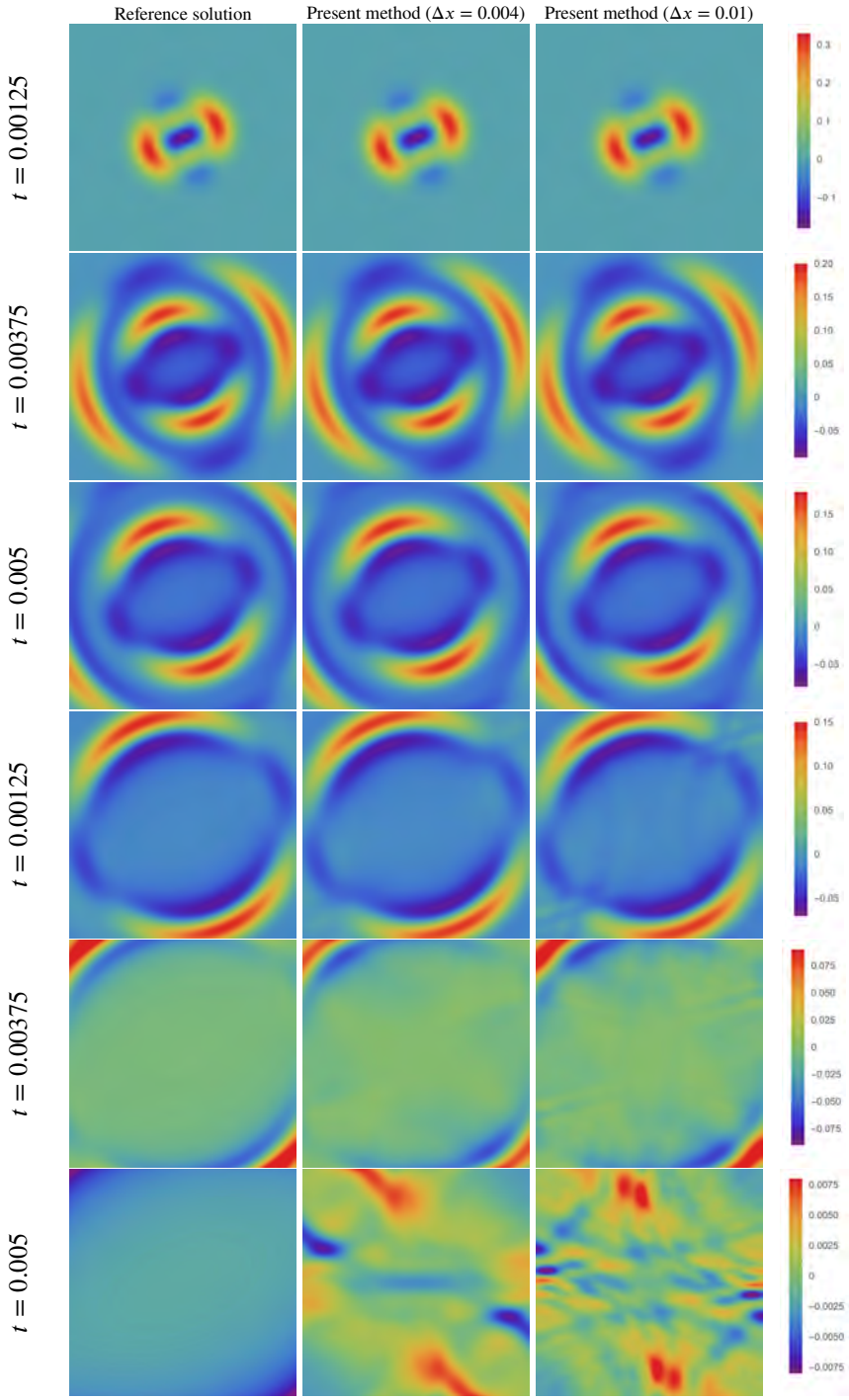

Figure 7: The results obtained for the propagation of pulse at different time instants in Example 1, Part A; the figure shows the contour of displacement along the x-axis, u, for $\Delta x = 0.004$ and $\Delta x = 0.01$.

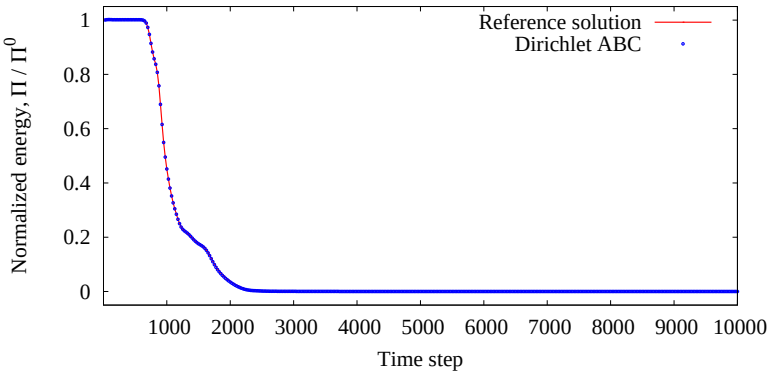

Figure 8: The variation of energy obtained by two models in Example 1, Part A; $\Delta x = 0.004$.

time. The normalization is again done with respect to $\Pi^0 = \Pi^0_{\text{ref}}$, the energy of the corresponding extended model at the beginning of the simulation. The energy difference is calculated by:

$$\Delta\Pi = \left|\Pi_{\text{ref}} - \Pi\right| \tag{72}$$

where Π_{ref} and Π correspond to the energy of the reference solution and the present model, respectively. The results in Fig. 9 elucidate, quantitatively, that making use of a finer grid size for the model contributes to a higher accuracy. To check the convergence rate of the approach, we define L_2 error norm of energy, e, as:

$$e = \sqrt{\frac{\sum_n \left(\Pi^n_{\text{ref}} - \Pi^n\right)^2}{\sum_n (\Pi^n_{\text{ref}})^2}} \tag{73}$$

where $\Pi^n = \Pi(t_n)$, and the above summation runs over the number of steps; in this study 3000 steps is taken into account. The obtained results of the convergence study are reported in Table 1. It again approves the convergent behavior of the approach similar to the conclusion made for Fig. 9.

To sum up, the proposed absorbing technique performs well in time, exhibits suitable results with a proper accuracy (at the level of energy), and also preserves a stable behavior as the simulator progresses in time.

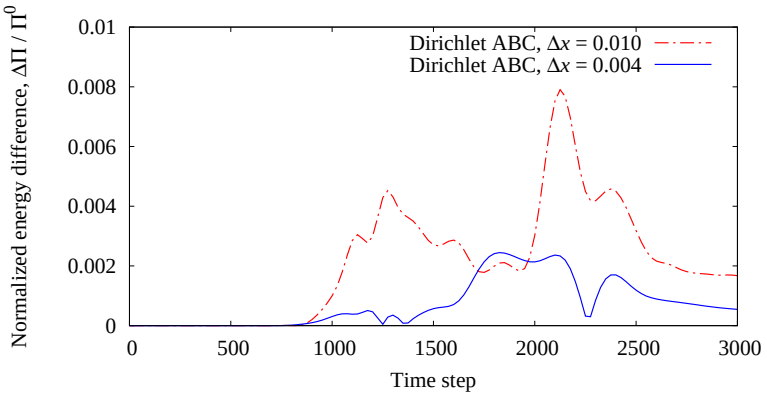

Figure 9: The variation of the normalized energy difference in time using different sizes of grid spacing in Example 1, Part A.

Table 1: The convergence study in Example 1, Part A.

Δx	Error norm, e
0.010	0.00515067
0.004	0.00193391

Part B: FEM solution

To check the application of the proposed method to a standard FEM solver, we solve the same problem as in Part A with FEM. The computational domain, taken the same size as Part A, is discretized with a Cartesian mesh of bilinear quadrilateral elements, with the same size as the grid spacing, Δx in previous part. For the reference solution, we employ an extended domain as in Part A, on which the problem is solved using an standard FEM solver. Both solvers use the velocity-Verlet algorithm as referred to in Alg. 1. To make a better comparison with the available methods in the literature, we solve the problem using the standard 1st order ABC method [54].

Here we report the difference in the mechanical energy of the system between the proposed method and the 1st order ABC method inside the computational domain. The difference is again normalized with respect to the energy of the system at the beginning of the simulation, Π^0. It is very important to note that in previous part of this example, we tried to implement the 1st order ABC method in the FPM solver; however, the method was completely unstable, leaving us no other choice than the proposed method for solution of the unbounded domain using an FPM scheme.

The results depicted in Fig. 10 show that while the 1st order ABC method is superior in a very short span of the time in the middle of simulation, the proposed method performs better, especially in the final stage of the simulation, when the majority of the energy is radiated towards the exterior domain.

6.2. Example 2: wave motion in an unbounded domain with scatterers

The main target in this example is to demonstrate the performance of the present method in the solution of an elastic wave motion problem in presence of scatterers inside the computational domain. The scatterers reflect waves at different angles of incidence; hence, such a problem is harder to solve and has more similarity with real-world engineering problems. For a better comparison, we use the same computational and extended domains as in Example 1, and add two circular scatterers. These scatterers are positioned asymmetrically within the computational domain at $\langle 0.25, 0.25\rangle$ and $\langle 0, -0.3\rangle$, both with a radius of 0.1. For the initial condition of the system, we choose a superposition of two Gaussian bell shapes, as in Eq. (71), but centered at $\langle \pm 0.1, 0\rangle$.

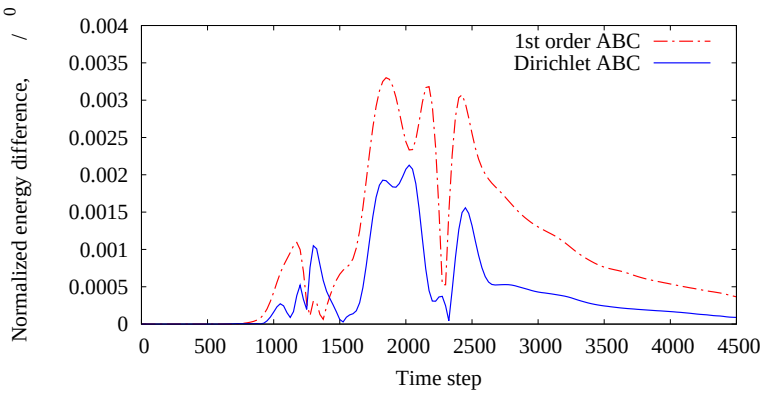

Figure 10: The variation of the normalized energy difference in time between the Dirichlet ABC and the 1st order ABC in Example 1, Part B.

The initial displacement along the x-axis, as well as the aforementioned scatterers are depicted in Fig. 11. Homogenous Dirichlet condition is imposed on the scatterers.

The computational and extended domains are discretized using a Cartesian grid with $\Delta x = 0.004$. The solver is run for 3000 steps with a time increment of $\Delta t = 5 \times 10^{-6}$ as before, leading to a final time of $T = 0.015$.

The contour plots of displacement along the x-axis obtained by both models at different time instants are presented in Fig. 12. It can be observed that the solution obtained by the present model conforms well to that of the reference solution. The absorbing technique is performing appropriately, and no accountable spurious reflections can be observed in the results, while the reflection of the waves from the scatterers creates a much more complex pattern and waves with very different incidence angles reach the boundaries of the computational domain. Even in the last time instant, $t = 0.015$, still rather good conformity is seen between the results. Nonetheless, the present absorbing technique is capable of guiding the waves towards the exterior domain in an appropriate manner, so that the solution obtained by the present model resembles that of the reference solution.

Similar to the previous example, the stability of the numerical solution for a long-term computational process is examined. To this respect, the variation of normalized energy (corresponding to the computational domain) for 10 000 time steps is reported

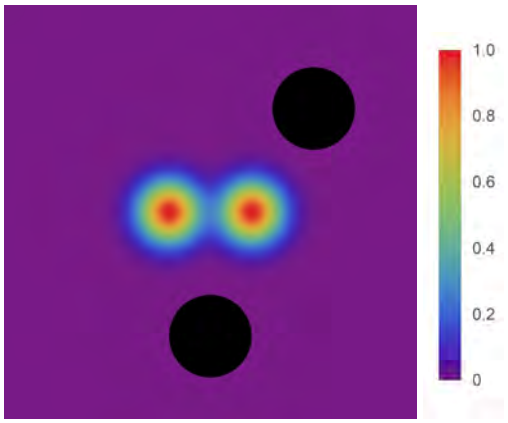

Figure 11: The initial condition in Example 2; the figure shows the displacement along the x-axis, u, taking $\Delta x = 0.004$ in addition to the scatterers shown as black disks.

Table 2: The convergence study in Example 2.

Δx	Error norm, e
0.010	0.01605040
0.004	0.00333814

in Fig. 13 (even though we have continued the simulation up to 100 000 steps). The energy is normalized with respect to the initial energy of the system. As can be seen, the energy dissipation rate in monotonic, and no instability (due to long-term calculations) can be concluded from the trend of variation. It should be remarked here that in this example, due to presence of the scatterers, the energy leaves the domain at a slower rate, compared to Example 1.

As in previous example, we report the normalized energy difference between the proposed method and the reference solution in Fig. 14 for two different grid sizes, Δx, of 0.01 and 0.004. As expected, the finer model is superior in terms of energy difference, especially in last steps of the simulation. For a quantitative comparison, the L_2 energy error norm, e, defined in Eq. (73) for both grid sizes is reported in Table 2, which shows better performance of the method when used with a finer grid size. The results, again, approve the conclusion made in the previous example about the proposed method.

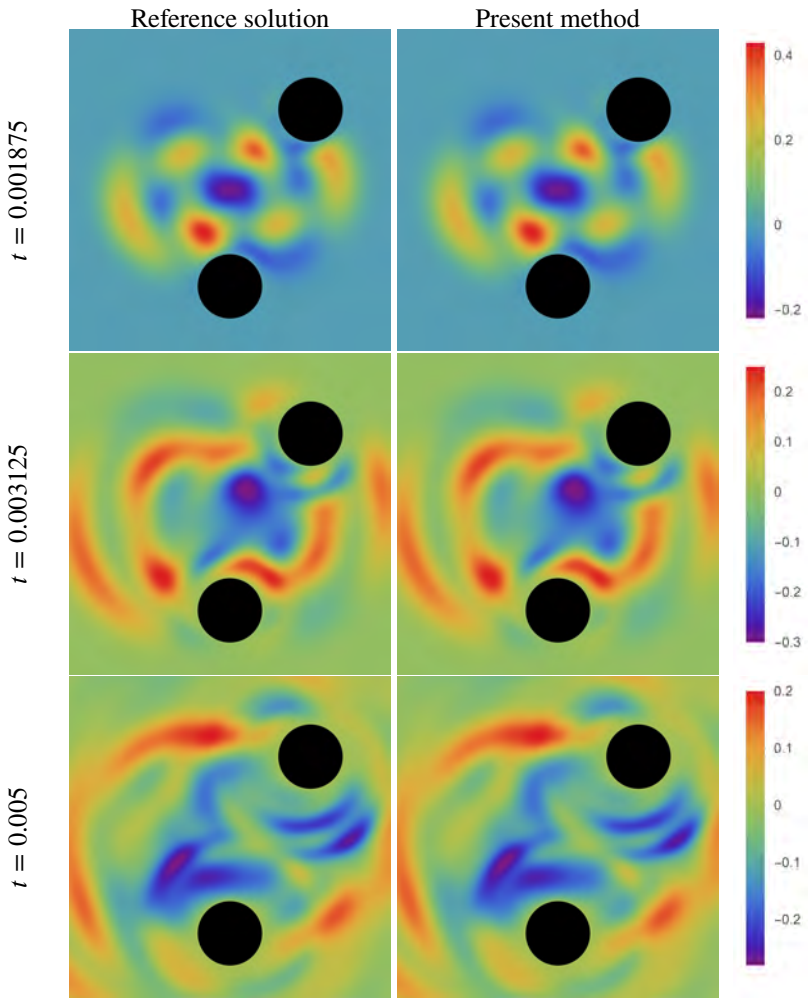

Figure 12: The results obtained for the propagation of pulse at different time instants in Example 2; the figure shows the contour of displacement along the x-axis, u, taking $\Delta x = 0.004$.

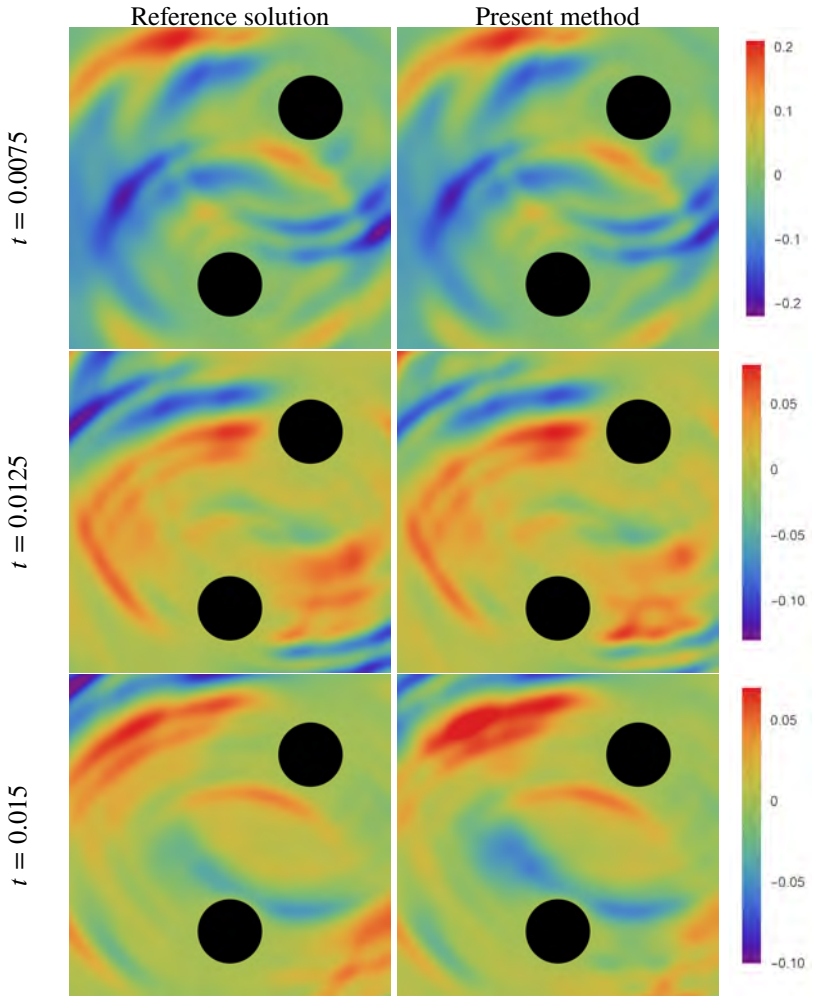

Figure 12: (continued)

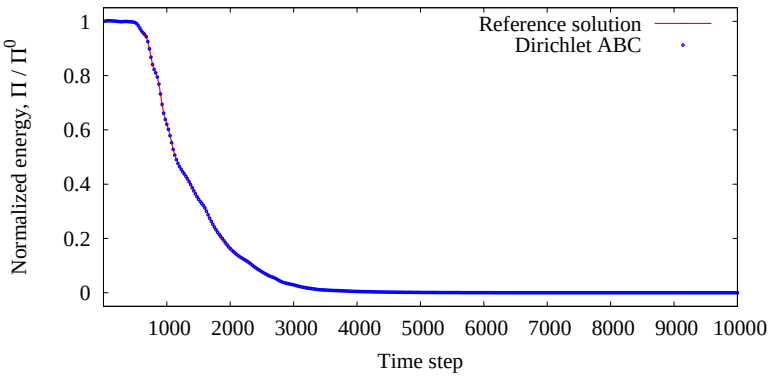

Figure 13: The variation of energy obtained by the present method in Example 2.

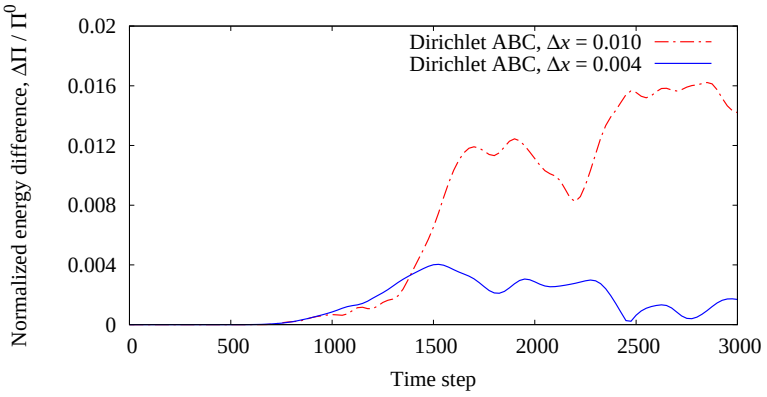

Figure 14: The variation of the normalized energy difference in time using different sizes of grid spacing in Example 2.

7. Conclusion

A Dirichlet-type ABC for unbounded elastodynamic problems is presented. The proposed method is local in space and time and does not employ any auxiliary variables or spatial derivatives of the field variables. It is equally well applicable to the FEM and the meshless FPM methods, as it does not directly involve with the solution in the near field. This makes its implementation very easy, even in existing codes. The method makes use of a series of plane waves adjusted to radiate energy towards the exterior domain, based on residual-free EBFs. A local collocation scheme is employed to construct the required vectors for calculation of ABCs at the beginning of the simulation. The ABCs are then used at each time step to update the field variables on the truncating boundary. A rather detailed investigation of the method is performed in a series of numerical examples. The accuracy of the method is shown by reporting the relative energy difference of the method with a reference solution on an extended domain. In the FEM example, the accuracy of the proposed method is compared with that of the standard 1st order ABC method. It is interesting to report that our experiences show that the 1st order ABC method is unstable in FPM scheme, while the proposed method can serve as a viable solution for treating problems with unbounded domains with a consistent formulation. Another example, incorporating scatterers inside the computational domain is investigated. While existence of the scatterers causes a very complex pattern of waves, reaching the truncating boundary with different angles of incidence, the proposed method is capable of appropriately transmit the energy towards the exterior domain, without accountable spurious reflections.

Acknowledgments

The financial support of the University of Padova under research contract BIRD2017 NR. 175705/17 is gratefully acknowledged by Mirco Zaccariotto, and under research contract BIRD2018 NR.183703/18 by Ugo Galvanetto.

References

[1] G. B. Whitham, Linear and nonlinear waves, Vol. 42, John Wiley & Sons, 2011.

[2] J. P. Wolf, Soil-structure-interaction analysis in time domain, Nuclear engineering and design 111 (3) (1989) 381–393.

[3] J. H. Lee, J. L. Tassoulas, Consistent transmitting boundary with continued-fraction absorbing boundary conditions for analysis of soil–structure interaction in a layered half-space, Computer Methods in Applied Mechanics and Engineering 200 (13-16) (2011) 1509–1525.

[4] H. Bao, J. Bielak, O. Ghattas, L. F. Kallivokas, D. R. O'Hallaron, J. R. Shewchuk, J. Xu, Large-scale simulation of elastic wave propagation in heterogeneous media on parallel computers, Computer methods in applied mechanics and engineering 152 (1-2) (1998) 85–102.

[5] D. Rabinovich, S. Vigdergauz, D. Givoli, T. Hagstrom, J. Bielak, Optimized first-order absorbing boundary conditions for anisotropic elastodynamics, Computer Methods in Applied Mechanics and Engineering 350 (2019) 719–749.

[6] J. H. Lee, J. L. Tassoulas, Root-finding absorbing boundary conditions for scalar and elastic waves in infinite media, Computer Methods in Applied Mechanics and Engineering 346 (2019) 592–611.

[7] A. Shojaei, U. Galvanetto, T. Rabczuk, A. Jenabi, M. Zaccariotto, A generalized finite difference method based on the peridynamic differential operator for the solution of problems in bounded and unbounded domains, Computer Methods in Applied Mechanics and Engineering 343 (2019) 100–126.

[8] M. Zhao, L. Wu, X. Du, Z. Zhong, C. Xu, L. Li, Stable high-order absorbing boundary condition based on new continued fraction for scalar wave propagation in unbounded multilayer media, Computer Methods in Applied Mechanics and Engineering 334 (2018) 111–137.

[9] D. Rabinovich, D. Givoli, J. Bielak, T. Hagstrom, The double absorbing boundary method for elastodynamics in homogeneous and layered media, Advanced Modeling and Simulation in Engineering Sciences 2 (1) (2015) 3.

[10] D. Baffet, J. Bielak, D. Givoli, T. Hagstrom, D. Rabinovich, Long-time stable high-order absorbing boundary conditions for elastodynamics, Computer Methods in Applied Mechanics and Engineering 241 (2012) 20–37.

[11] J. Lysmer, R. L. Kuhlemeyer, Finite dynamic model for infinite media, Journal of the Engineering Mechanics Division 95 (4) (1969) 859–878.

[12] X. Ma, Y. Li, J. Song, A stable auxiliary differential equation perfectly matched layer condition combined with low-dispersive symplectic methods for solving second-order elastic wave equations, Geophysics 84 (4) (2019) T193–T206.

[13] B. Engquist, A. Majda, Absorbing boundary conditions for numerical simulation of waves, Proceedings of the National Academy of Sciences 74 (5) (1977) 1765–1766.

[14] J.-F. Semblat, L. Lenti, A. Gandomzadeh, A simple multi-directional absorbing layer method to simulate elastic wave propagation in unbounded domains, International Journal for Numerical Methods in Engineering 85 (12) (2011) 1543–1563.

[15] S.-H. Park, J. L. Tassoulas, A discontinuous galerkin method for transient analysis of wave propagation in unbounded domains, Computer Methods in Applied Mechanics and Engineering 191 (36) (2002) 3983–4011.

[16] J. Dominguez, Boundary elements in dynamics, Wit Press, 1993.

[17] D. Givoli, High-order local non-reflecting boundary conditions: a review, Wave motion 39 (4) (2004) 319–326.

[18] D. Givoli, Non-reflecting boundary conditions, Journal of computational physics 94 (1) (1991) 1–29.

[19] S. V. Tsynkov, Numerical solution of problems on unbounded domains. a review, Applied Numerical Mathematics 27 (4) (1998) 465–532.

[20] I. Harari, T. J. Hughes, Analysis of continuous formulations underlying the computation of time-harmonic acoustics in exterior domains, Computer Methods in Applied Mechanics and Engineering 97 (1) (1992) 103–124.

[21] I. Harari, T. J. Hughes, Galerkin/least-squares finite element methods for the reduced wave equation with non-reflecting boundary conditions in unbounded domains, Computer methods in applied mechanics and engineering 98 (3) (1992) 411–454.

[22] A. Shojaei, B. Boroomand, E. Soleimanifar, A meshless method for unbounded acoustic problems, The Journal of the Acoustical Society of America 139 (5) (2016) 2613–2623.

[23] A. El Kacimi, O. Laghrouche, D. Ouazar, M. Mohamed, M. Seaid, J. Trevelyan, Enhanced conformal perfectly matched layers for bernstein–bézier finite element modelling of short wave scattering, Computer Methods in Applied Mechanics and Engineering 355 (2019) 614–638.

[24] U. Basu, A. K. Chopra, Perfectly matched layers for transient elastodynamics of unbounded domains, International Journal for Numerical Methods in Engineering 59 (8) (2004) 1039–1074.

[25] A. Fathi, L. F. Kallivokas, B. Poursartip, Full-waveform inversion in three-dimensional pml-truncated elastic media, Computer Methods in Applied Mechanics and Engineering 296 (2015) 39–72.

[26] E. Salete, J. J. Benito, F. Ureña, L. Gavete, M. Ureña, A. García, Stability of perfectly matched layer regions in generalized finite difference method for wave problems, Journal of Computational and Applied Mathematics 312 (2017) 231–239.

[27] X. Liu, Y. Liu, Z.-M. Ren, X.-H. Cai, B. Li, S.-G. Xu, L.-K. Zhou, Hybrid absorbing boundary condition for three-dimensional elastic wave modeling, Applied Geophysics 14 (2) (2017) 270–278.

[28] J.-P. Berenger, A perfectly matched layer for the absorption of electromagnetic waves, Journal of computational physics 114 (2) (1994) 185–200.

[29] F. Q. Hu, Development of pml absorbing boundary conditions for computational aeroacoustics: A progress review, Computers & Fluids 37 (4) (2008) 336–348.

[30] K. Duru, G. Kreiss, Numerical interaction of boundary waves with perfectly matched layers in two space dimensional elastic waveguides, Wave Motion 51 (3) (2014) 445–465.

[31] F. Collino, et al., High order absorbing boundary conditions for wave propagation models. straight line boundary and corner cases, in: Second International Conference on Mathematical and Numerical Aspects of Wave Propagation (Newark, DE, 1993), SIAM Philadelphia, PA, 1993, pp. 161–171.

[32] A. Bayliss, E. Turkel, Radiation boundary conditions for wave-like equations, Communications on Pure and applied Mathematics 33 (6) (1980) 707–725.

[33] M. J. Grote, Local nonreflecting boundary condition for maxwellâĂŹs equations, Computer methods in applied mechanics and engineering 195 (29-32) (2006) 3691–3708.

[34] D. Rabinovich, D. Givoli, J. Bielak, T. Hagstrom, The double absorbing boundary method for a class of anisotropic elastic media, Computer Methods in Applied Mechanics and Engineering 315 (2017) 190–221.

[35] D. Rabinovich, D. Givoli, E. Bécache, Comparison of high-order absorbing boundary conditions and perfectly matched layers in the frequency domain, International Journal for Numerical Methods in Biomedical Engineering 26 (10) (2010) 1351–1369.

[36] G. Lancioni, Numerical comparison of high-order absorbing boundary conditions and perfectly matched layers for a dispersive one-dimensional medium, Computer Methods in Applied Mechanics and Engineering 209 (2012) 74–86.

[37] A. Shojaei, F. Mossaiby, M. Zaccariotto, U. Galvanetto, A local collocation method to construct dirichlet-type absorbing boundary conditions for transient scalar wave propagation problems, Computer Methods in Applied Mechanics and Engineering 356 (2019) 629–651.

[38] E. Oñate, F. Perazzo, J. Miquel, A finite point method for elasticity problems, Computers & Structures 79 (22-25) (2001) 2151–2163.

[39] A. Shojaei, F. Mossaiby, M. Zaccariotto, U. Galvanetto, The meshless finite point method for transient elastodynamic problems, Acta Mechanica 228 (10) (2017) 3581–3593.

[40] B. Boroomand, A. Tabatabaei, E. Onate, Simple modifications for stabilization of the finite point method, International Journal for Numerical Methods in Engineering 63 (3) (2005) 351–379.

[41] A. Shojaei, T. Mudric, M. Zaccariotto, U. Galvanetto, A coupled meshless finite point/peridynamic method for 2d dynamic fracture analysis, International Journal of Mechanical Sciences 119 (2016) 419–431.

[42] A. Shojaei, F. Mossaiby, M. Zaccariotto, U. Galvanetto, An adaptive multi-grid peridynamic method for dynamic fracture analysis, International Journal of Mechanical Sciences 144 (2018) 600–617.

[43] M. Zaccariotto, T. Mudric, D. Tomasi, A. Shojaei, U. Galvanetto, Coupling of fem meshes with peridynamic grids, Computer Methods in Applied Mechanics and Engineering 330 (2018) 471–497.

[44] S. Bazazzadeh, F. Mossaiby, A. Shojaei, An adaptive thermo-mechanical peridynamic model for fracture analysis in ceramics, Engineering Fracture Mechanics 223 (2020) 106708. doi:https://doi.org/10.1016/j.engfracmech.2019.106708.

[45] E. Perrey-Debain, J. Trevelyan, P. Bettess, P-wave and s-wave decomposition in boundary integral equation for plane elastodynamic problems, Communications in numerical methods in engineering 19 (12) (2003) 945–958.

[46] S. Hashemi, B. Boroomand, B. Movahedian, Exponential basis functions in space and time: A meshless method for 2d time dependent problems, Journal of Computational Physics 241 (2013) 526–545.

[47] A. Shojaei, B. Boroomand, F. Mossaiby, A simple meshless method for challenging engineering problems, Engineering Computations 32 (6) (2015) 1567.

[48] S. Mirfatah, B. Boroomand, E. Soleimanifar, On the solution of 3d problems in physics: From the geometry definition in cad to the solution by a meshless method, Journal of Computational Physics 393 (2019) 351–374.

[49] H. G. Feichtinger, K. Gröchenig, Theory and practice of irregular sampling, Wavelets: mathematics and applications 1994 (1994) 305–363.

[50] J. Bezanson, S. Karpinski, V. B. Shah, A. Edelman, Julia: A fast dynamic language for technical computing, arXiv preprint arXiv:1209.5145.

[51] F. Mossaiby, A. Shojaei, M. Zaccariotto, U. Galvanetto, OpenCL implementation of a high performance 3D peridynamic model on graphics accelerators, Computers & Mathematics with Applications 74 (8) (2017) 1856–1870.

[52] F. Mossaiby, M. Ghaderian, A preliminary study on the meshless local exponential basis functions method for nonlinear and variable coefficient PDEs, Engineering Computations 33 (8) (2016) 2238–2263.

[53] D. Rabinovich, D. Givoli, J. Bielak, T. Hagstrom, A finite element scheme with a high order absorbing boundary condition for elastodynamics, Computer Methods in Applied Mechanics and Engineering 200 (23-24) (2011) 2048–2066.

[54] B. Engquist, A. Majda, Radiation boundary conditions for acoustic and elastic wave calculations, Communications on pure and applied mathematics 32 (3) (1979) 313–357.